Hot Isostatic Pressing for Reduction of Defects in Additively Manufactured Inconel-718

Preliminary Simulation Approach and Results

Joshua M. Fody
Langley Research Center, Hampton, Virginia

Christapher G. Lang
Langley Research Center, Hampton, Virgnia

NASA STI Program Report Series

Since its founding, NASA has been dedicated to the advancement of aeronautics and space science. The NASA scientific and technical information (STI) program plays a key part in helping NASA maintain this important role.

The NASA STI program operates under the auspices of the Agency Chief Information Officer. It collects, organizes, provides for archiving, and disseminates NASA's STI. The NASA STI program provides access to the NTRS Registered and its public interface, the NASA Technical Reports Server, thus providing one of the largest collections of aeronautical and space science STI in the world. Results are published in both non-NASA channels and by NASA in the NASA STI Report Series, which includes the following report types:

- TECHNICAL PUBLICATION. Reports of completed research or a major significant phase of research that present the results of NASA Programs and include extensive data or theoretical analysis. Includes compilations of significant scientific and technical data and information deemed to be of continuing reference value. NASA counterpart of peer-reviewed formal professional papers but has less stringent limitations on manuscript length and extent of graphic presentations.

- TECHNICAL MEMORANDUM. Scientific and technical findings that are preliminary or of specialized interest, e.g., quick release reports, working papers, and bibliographies that contain minimal annotation. Does not contain extensive analysis.

- CONTRACTOR REPORT. Scientific and technical findings by NASA-sponsored contractors and grantees.

- CONFERENCE PUBLICATION. Collected papers from scientific and technical conferences, symposia, seminars, or other meetings sponsored or co-sponsored by NASA.

- SPECIAL PUBLICATION. Scientific, technical, or historical information from NASA programs, projects, and missions, often concerned with subjects having substantial public interest.

- TECHNICAL TRANSLATION. English-language translations of foreign scientific and technical material pertinent to NASA's mission.

Specialized services also include organizing and publishing research results, distributing specialized research announcements and feeds, providing information desk and personal search support, and enabling data exchange services.

For more information about the NASA STI program, see the following:

- Access the NASA STI program home page at http://www.sti.nasa.gov

- Help desk contact information:

https://www.sti.nasa.gov/sti-contact-form/

and select the "General" help request type.

Hot Isostatic Pressing for Reduction of Defects in Additively Manufactured Inconel-718

Preliminary Simulation Approach and Results

Joshua M. Fody
Langley Research Center, Hampton, Virginia

Christapher G. Lang
Langley Research Center, Hampton, Virgnia

Abstract

Selective laser melting (SLM) of Inconel-718 (IN718) is a promising advanced manufacturing technology; however, challenges exist for fracture-critical parts where pores induced during the manufacturing process reduce fatigue life of the material. Hot isostatic pressing (HIP) is a common post processing technique used to reduce the part porosity by exposing parts to high temperature and pressures. Pore closure depends on the pore shape, trapped gas, and HIP parameters, and the process can only be optimized by understanding the effect of these variables. An analysis capability is described to better understand the conditions necessary for pore closure, and the effect of several variables on porosity are explored and compared to a baseline case. The importance of valid material response models is identified as a significant factor in model accuracy; especially the creep material response model which, in the baseline case, predicts that creep strain accounts for 87.7% of the total strain at the conclusion of the HIP cycle. Lessons learned are described in addition to future work including model validation.

1.0 SYMBOLS

A	Creep rate coefficient
B	Plastic temperature sensitivity parameter
C	Plastic strain rate strength coefficient
E	Modulus of elasticity in tension
F	Deformation gradient tensor
F_A	Boundary load vector
F_{el}	Elastic deformation gradient tensor
F_{cr}	Creep deformation function
F_{inel}	Inelastic deformation gradient tensor
F_{pl}	Plastic deformation gradient tensor
F_v	Volume force vector
F_y	Plastic Yield Function
I	Identity matrix
J	Jacobian determinant
K	Bulk modulus
k	Plastic strength coefficient
M_{Ar}	Argon molar mass
m	Plastic thermal softening exponent
n_{cr}	Creep stress exponent
n^D	Deviatoric tensor
n_{JC}	Plastic hardening exponent
n_s	Surface normal vector
P_{pore}	Pore pressure
p	Pressure
p_w	Auxiliary pressure variable
Q	Creep activation energy
Q_p	Plastic Potential
R	Gas constant
S	Second Piola-Kirchhoff stress tensor
S_{ext}	External stress
T	Temperature

T_{ps}	Plastic thermal softening term
t	Time
u	Displacement field
$V_{0\,pore}$	Initial pore volume
V_{pore}	Pore volume
X	Reference frame coordinate
x	Spatial frame coordinate
$\dot{\epsilon}_{cr}$	Creep strain rate
$\dot{\epsilon}_{cr\_eff}$	Effective creep strain rate
$\dot{\epsilon}_0$	Plastic reference strain rate
ϵ	Strain tensor
ϵ_{el}	Elastic strain
ϵ_{pe}	Effective plastic strain
$\dot{\epsilon}_p$	Plastic strain rate
$\dot{\epsilon}_{pe}$	Effective plastic strain rate
λ	Plastic multiplier
ν	Poisson's ratio
ρ	Density
ρ_{Ar}	Argon density
σ	Stress
σ_{el}	Elastic stress
$\sigma_{el\,vol}$	Elastic volume stress
σ_{mises}	Von Mises Stress
σ_{ref}	Reference stress
σ_{ys0}	Initial yield stress
σ_{ys}	Plastic yield stress

Table of Contents

Table of Figures

2.0 INTRODUCTION

2.1 Motivation

Selective laser melting (SLM) of Inconel 718 is a promising advanced manufacturing technology for producing on-demand and complex aerospace components for high temperature and high strength applications. However, challenges exist for fracture-critical parts where pores induced during the manufacturing process act as stress risers and crack initiation sites leading to a significantly reduced fatigue life of the material. Hot isostatic pressing (HIP) is performed after the SLM process to reduce the part porosity. During HIP, the internal pores close and fuse under the elevated temperature and pressure. HIP parameters include the temperature, pressure, and duration of the process. A majority of the internal pores are expected to be closed during HIP, and pore closure depends on the pore shape, trapped gas, and HIP parameters. An analysis capability is created to better understand the conditions necessary for pore closure. Model validation was planned using X-ray computed tomography data of samples before and after HIP; however, due to restricted laboratory access caused by the Covid-19 pandemic validation work was not completed. Model validation is addressed in section 7.2 Future Work.

2.2 Background

Previous studies document related efforts on experimental characterization and analysis approaches. The HIP for SLM Inconel parts has been shown to be effective at reducing porosity using X-ray CT measurements (Tillmann, et al. 2017), (Kreitcberg and et al. 2017). Causes for porosity which remained after HIP were identified as surface connected pores and trapped argon gas. Mechanical properties have also been measured to understand the impact of HIP (Kreitcberg and et al. 2017), (Finfrock and et al. 2018), and additional heat treatments are needed to recover optimal properties. Finally, characterization of porosity before and after HIP was performed for electron beam melting of Ti-6Al-4V, and HIP was shown to reduce porosity and improve fatigue life (Tammas-Williams and et al. 2016). However, surface connected porosity persisted through the HIP process which can significantly extend into the part volume depending on the manufacturing process.

Analytical studies have been performed related to material models and part-scale deformation for the HIP process. A combined plastic and viscoplastic model was developed for HIP powder densification (Wikman and et al. 2000), (Sanchez and et al. 2002). Finite element analysis has been performed for the HIP process to predict the part-scale deformation and final part geometry (Du and et al. 2019). The objective of this study is to model pore closure during the HIP process of SLM IN718 parts which incorporates the appropriate material model at the length scale of a single pore. A closely related study was a finite element analysis to predict pore closure for hot rolling of steel (Joo and et al. 2014). The initial pore shape for the hot rolling process was identified as a critical factor for densification.

2.3 Objective

The objective of the research is to develop an analysis capability for predicting pore closure as a function of the HIP process conditions and pore geometry. A thermal-mechanical finite element

analysis is created with HIP conditions (temperature, pressure, and time), pore size and shape, and material model at elevated temperature as input data. A single pore is considered in this effort, and pore closure as a function of the process parameters is studied.

3.0 APPROACH

Finite element modeling for this analysis was conducted using COMSOL Multiphysics® commercial software. The 2-D model geometry, mesh, physics, and solver settings are described in detail below. Additional descriptions of a 3-D spherical model follow with emphasis only on aspects of those models that differ from the 2-D model.

3.1 2-D Model Description

Geometry and mesh:

The 2-D finite element model was the primary model used for analysis. The 2-D model was a planar geometry consisted of a square representative solid volume surrounding a circular pore. For all cases analyzed, the pore was much smaller in size than the representative volume. The following geometry and mesh discussion and images are taken from the baseline model. Baseline model parameter settings can be found in Table 5. The configurations for all cases were the same, only the parameter settings changed; therefore, this discussion is relevant to all cases run.

The baseline 2-D model mesh consisted of a total of 21,344 mesh vertices and 21,160 mesh elements. All the elements were quadrilateral and were produced by first defining mesh nodes on the round pore wall and then mapping those nodes outward to the rectangular surface. This mapping produced a mesh pattern like spokes on a bicycle wheel. These long and narrow elements were then divided radially to produce elements that were more square or rectangular. The divisions were specified along lines of model symmetry emanating from the pore wall diagonally outward to the corners of the square representative volume external boundary. A full view of the baseline 2-D model showing mesh elements can be seen in Figure 1.
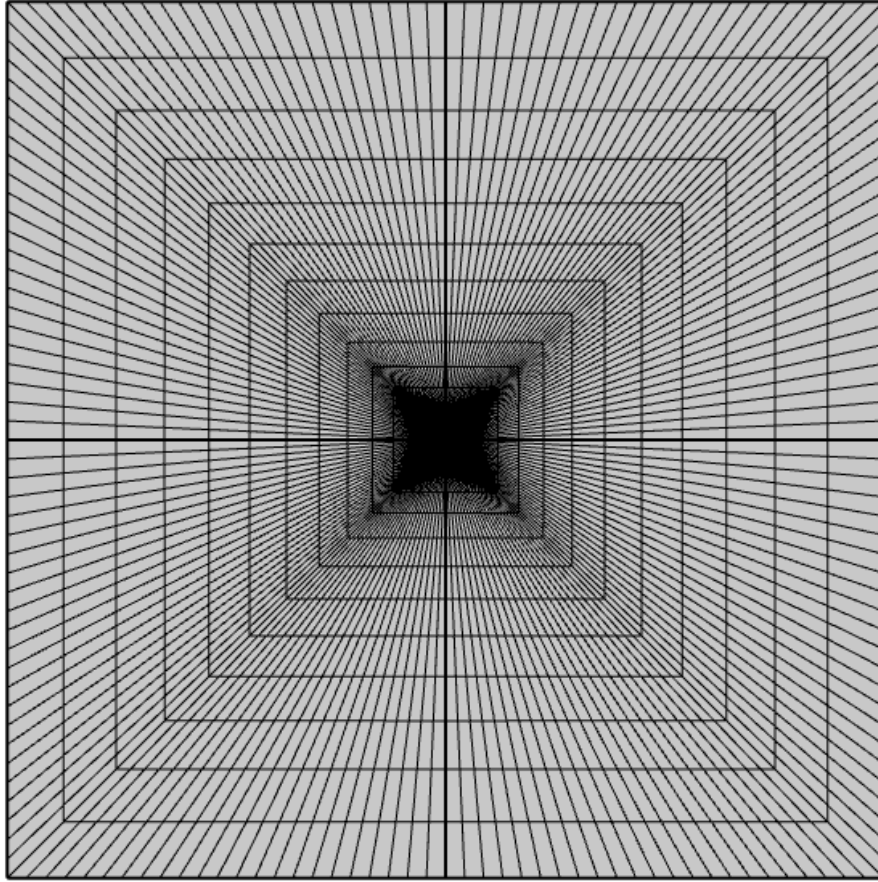
Figure 1: View of the full meshed 2-D model geometry for the baseline case. The relatively tiny central pore is not visible at this scale.

The number of edge elements defining the mesh were specified on the pore wall and along the lines of model symmetry. Four distinct regions of mesh density, one along the pore wall and three regions of radial mesh density – high, medium, and low – with the high density near the pore wall and low near the outer boundary of the solid volume were specified. Edge element count at the pore wall and in the high-density region were specified using a parameter called "mesh count". Mesh count for the baseline case was 70; edge elements in the high-density region were specified by rounding the product of mesh count and a decimal fraction so that mesh count could be varied in other studies in order to parametrically assess the effect of mesh density on model results. Edge element count in the medium and low-density regions were specified as integers. Radial edge elements were spaced according to a growth ratio – the ratio of the size of the first and final edge element over the region bounds. This growth ratio increased element size further from the pore wall radially. The mesh regions for the 2-D model are described in Table 1 with the decimal fraction and geometric bounds of the region given for the lines within each; the number of edge elements within the bounds and the total resulting number of field mesh elements for each region are also given for the baseline case.

Table 1: Mesh density regions for the baseline 2-D model.

Mesh Region	Pore Wall	High	Medium	Low
Decimal Fraction	2.6	1	N/A	N/A
Bounds	Total Perimeter	Pore – 90 μm	90 μm – 8 mm	8mm - Exterior
Edge Elements	184	70	30	15
Growth Ratio	1	10	50	50
Total Field Elements	(High Region)	12,880	5,520	2,760

Views of the 2-D model mesh that are zoomed in to show mesh region interfaces are seen in Figure 2. Note the transition in the shape of the radial divisions from round to square as the mesh progresses from the pore wall to the external solid volume boundary.
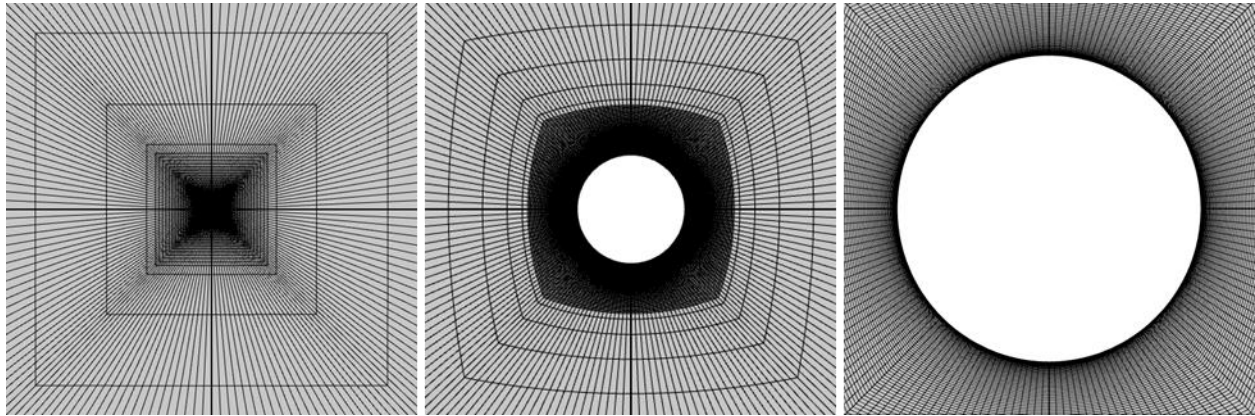
Figure 2: 2-D model baseline mesh regions. Showing interface between low and medium density (left), medium and high (center), and the pore wall (right).

Structural mechanics approach:

A total Lagrangian formulation is utilized for this simulation which employs a two-frame approach for calculating deformation. Equation 1 demonstrates the relationship between frames; x is the spatial coordinate, X is the reference frame coordinate, and u is the displacement vector.

Equation 1: Deformation of spatial frame coordinates relative to the reference frame as per the total Lagrangian approach.

$$x = X + u(X, t)$$

The governing equation of motion is implemented as shown in Equation 2.

Equation 2: Governing equation of motion.

$$\nabla \cdot (FS)^T + F_v = \rho_0 \frac{\partial u^2}{\partial^2 t} = 0$$

Here, F_v is the volume force vector and has components in the spatial frame but is given with respect to the undeformed volume, F is the deformation gradient tensor, and S is the stress tensor. A quasi-static transient assumption is made, which specifies that no second order time derivatives are calculated in order to help the solver to converge; this assumption is appropriate given the relatively slow rates of displacement in the analysis. Accordingly, the force displacement term on the right-hand side of the governing equation of motion is neglected.

The deformation gradient tensor describes the deformation of the spatial coordinates relative to the reference frame as shown in Equation 3.

Equation 3: Deformation gradient tensor.

$$F = \frac{\partial x}{\partial X} = \nabla u + I$$

Specifically, S is the symmetric second Piola-Kirchhoff stress tensor with both force and area represented in the reference frame. S can represent all contributions to deformation in a linear relationship between the elastic deviatoric stress σ_{el} and inelastic deformation gradient as shown in Equation 4. The linear relationship was selected due to the reduced computational load and is appropriate as the vast majority of the deformation contribution is accounted for by the inelastic model components.

Equation 4: Stress tensor relating linear elastic and inelastic contributions.

$$S = S_{ext} + JF^{-1}{}_{inel} dev(\sigma_{el}) F^{-T}{}_{inel}$$

S_{ext} is the external applied stress, and J is the Jacobian determinant and relates to compressibility, where J = 1 would indicate a fully incompressible material. The deviatoric elastic stress component can be described further by Equation 5.

Equation 5: The deviatoric stress component with mixed pressure formulation.

$$dev(\sigma_{el}) = \sigma_{el} - \sigma_{el\,vol} = \sigma_{el} - (p + p_w)I$$

Where the elastic stress σ_{el} and elastic volume stress component $\sigma_{el\,vol}$ are determined from the elastic strain tensor ε_{el} as below.

$$\sigma_{el} = C{:}\epsilon_{el}$$

$$\sigma_{el\,vol} = (p + p_w)I = \left(\frac{1}{3} trace(C{:}\epsilon_{el}) + p_w\right)I$$

I is the identity matrix, and C is the elasticity tensor containing the bulk modulus E and Poisson's ratio ν. Note the addition of the auxiliary pressure variable p_w in the elastic volume stress formulation. This auxiliary pressure variable is implemented in order to offset error accumulation in the calculation of volumetric strain due to the high bulk modulus of nearly incompressible IN718 and finite resolution of the discrete model interpolations. The auxiliary pressure variable is treated as an additional dependent variable with a linear shape function, one order less than the rest of the physics, and is constrained according to the following relationship.

$$\frac{p_w - p}{K} = 0$$

K is the bulk modulus and is used for the purposes of scaling the pressure term to an order of magnitude nearer to the displacement. The elastic strain tensor is derived from the elastic deformation gradient tensor, following the Green-Lagrange strain tensor form as shown in Equation 6.

Equation 6: Green-Lagrange derivation of the elastic strain tensor and large plastic strains decomposition.

$$\epsilon_{el} = \frac{1}{2}\left(F_{el}{}^{T}F_{el} - I\right)$$

The elastic deformation gradient tensor F_{el} is derived from the total deformation gradient tensor F and plastic and creep gradient tensors as shown below.

$$F_{el} = FF_{pl}{}^{-1}F_{cr}{}^{-1}$$

The inelastic gradient tensor components are known from the plastic and creep material models, described shortly, and related by multiplication of the elastic and inelastic deformation gradients. This multiplicative decomposition of the deformation gradient is most appropriate for large plastic strains, as are observed in this study, as opposed to the additive decomposition of strains which is better suited for small strains.

The total strain tensor is defined following the Lagrange-Green form and related to the displacement field according to Equation 7.

Equation 7: Total strain tensor and displacement field relationship.

$$\epsilon = \frac{1}{2}(F^{T}F - I) = \frac{1}{2}\left((\nabla u)^{T} + \nabla u + (\nabla u)^{T}\nabla u\right)$$

For the 2-D model, the plane strain assumption is followed such that out of plane strain components are null as per Equation 8. Out of plane stress components are calculated assuming an out of plane thickness of 1 m.

Equation 8: Plane strain assumption.

$$\epsilon_z = \epsilon_{yz} = \epsilon_{xz} = 0$$

Much of the structural mechanics approach described here was drawn from helpful implementation descriptions given in the COMSOL software user's manual (COMSOL Multiphysics (R) v. 5.5 2019).

Plasticity Model:

In keeping with the large plastic strains decomposition approach referenced in Equation 6, an appropriate isotropic plastic flow rule was selected for this analysis. This flow rule is formulated as the Lie derivative of the elastic left Cauchy-Green deformation tensor; the final form as implemented is given in Equation 9.

Equation 9: Isotropic flow rule for large plastic strains and conditions.

$$JF\left(\dot{F_{pl}}^{-1}F_{pl}^{-1} + F_{pl}^{-1}\dot{F_{pl}}^{-1}\right) = -2\lambda\frac{\partial Q_p}{\partial S}FF_{pl}^{-2}$$

$\dot{F_{pl}}^{-1}$ is the reciprocal of the plastic deformation gradient rate tensor. The plastic potential Q_p is solved for after the plastic multiplier λ is determined using the yield function F_y – calculated by the Johnson-Cook material model – and the following Kuhn-Tucker conditions:

$$\lambda \geq 0, \qquad F_y \leq 0, \qquad \lambda F_y = 0$$

The plastic material model used for this analysis was based on the well-known Johnson-Cook formulation. Due to time and center access limitation, material properties test data was not generated for IN718 at temperature and loading conditions relevant to this study. The Johnson-Cook model was selected primarily because there is a large amount of readily available literature providing parameters for various materials, including IN718 Model parameters selected for this analysis leaned heavily on values found in (Iturbe, et al. 2017) including the adaptation of a novel thermal softening term developed in that work. Plasticity model parameters developed in the Iturbe publication were developed using IN718 uniaxial compression test data for temperatures in the range 21–1050 °C and strain rates $1 - 100$ s^{-1}. The Johnson-Cook model implementation is described in Equation 10.

Equation 10: Plastic yield function and Johnson-Cook material model implementation.

$$F_y = \sigma_{mises} - \sigma_{ys} \leq 0$$

$$\sigma_{ys} = \left(\sigma_{ys0} + k(\epsilon_{pe})^{n_{JC}}\right)\left(1 + C * \log\left(\frac{\dot{\epsilon}_{pe}}{\dot{\epsilon}_0}\right)\right)T_{ps}$$

$$T_{ps} = \left(\frac{1}{1 + \exp^{-m(T-B)}}\right)$$

$$\dot{\epsilon}_{pe} = \sqrt{\frac{2}{3}dev(\dot{\epsilon}_p):dev(\dot{\epsilon}_p)}$$

The Johnson-Cook model predicts plastic yield stress as a function of temperature effective plastic strain rate and effective plastic strain and is implemented into the structural model via the plastic yield function which assumes a Von Mises stress criterion for yielding. The effective plastic strain rate is defined from the plastic shear components. In this implementation, the logarithmic term is never permitted to achieve a value < 0; therefore, the reference strain rate value determines a quasistatic limit. As per the model parameters taken from (Iturbe, et al. 2017), temperature must be in units °C effective plastic strain rate in units 1/s and effective plastic strain is non dimensional. The plasticity model parameters assumed in this implementation are shown in Table 2.

Table 2: Johnson-Cook plasticity model parameters.

σ_{ys0}	k	n_{JC}	C	$\dot{\epsilon}_0$	m	B
MPa	MPa	1	1	1/s	1/°C	°C
1377	1243.5	0.6767	0.0045	1	0.00663	832.27

Creep Model:

The creep model for this analysis was the well-known Norton power law model combined with an Arrhenius type temperature dependent term. As with the plasticity model, material properties test data was not generated for IN718 at relevant temperature and loading conditions due to center access limitations. The Norton model was selected primarily because of the large amount of material parameters available in the literature. However, selecting appropriate creep model parameters from literature proved especially challenging; these challenges are covered in detail in the discussion section. Model parameters ultimately selected for this analysis leaned heavily on (Chaturvedi and Han 1989) and (Chavez, et al. 1994). The Norton model implementation is described in Equation 11.

Equation 11: Creep deformation function and the Norton power law implementation

$$F_{cr} = I + \epsilon_{cr}$$

$$\dot{\epsilon}_{cr} = \dot{\epsilon}_{cr\_eff} n^D$$

$$\dot{\epsilon}_{cr\_eff} = A \left(\frac{\sigma_{mises}}{\sigma_{ref}} \right)^{n_{cr}} e^{\frac{-Q}{RT}}$$

$$n^D = \frac{3 dev(\sigma)}{2 \sigma_{mises}}$$

The Norton power law creep model predicts effective creep strain rate as a function of effective stress – in this case Von Mises stress – normalized by the reference stress value and temperature using an Arrhenius type temperature dependent term. Input units for stress are Pa and K for temperature. The predicted effective creep strain rate is multiplied by the deviatoric tensor to produce the creep strain rate which is implemented into the structural model via the creep function. The creep model parameters assumed in this implementation are shown in Table 3.

Table 3: Norton power law creep model parameters.

A	σ_{ref}	n_{cr}	Q
1/s	Pa	1	J/mol
5.606	$1e^6$	3.84111	330296

Creep model parameters were primarily generated by fitting the temperature dependent Norton model to test data derived values found in (Chavez, et al. 1994). These reported values were linear extrapolations of the minimum creep rates found in tensile tests conducted on 0.5 in (1.27 cm) diameter IN600 alloy rod which had been annealed at 1416 °C (2581 °F) and forced air cooled. A total of 13 tests were conducted between 1349 °C (732 °F) and 1093 °C (1999 °F) with between 173 and 14.1 MPa applied stress. The minimum creep rate was reported in units of %/h. This rate was converted to units of 1/s for model implementation and treated as a scalar rate value. Fitting was performed using basic linear regression; the resultant model and reported data are shown in Figure 3 in units of 1/h as reported in the literature.
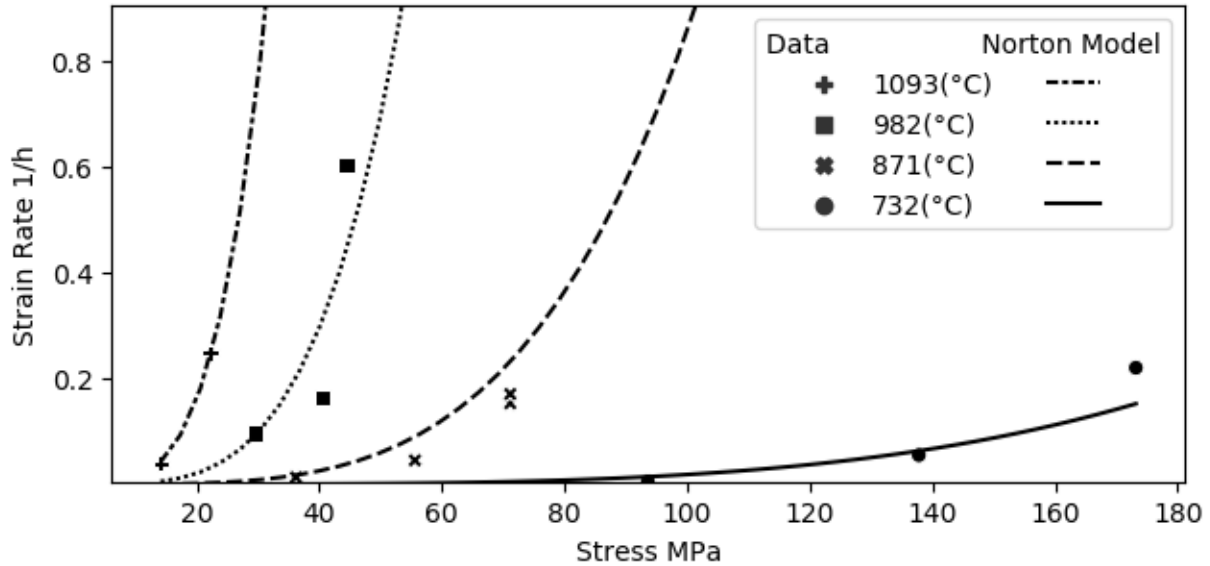
Figure 3: Temperature dependent Norton creep model used in this analysis compared to test data derived scalar minimum creep values reported in (Chavez, et al. 1994).

Boundary and initial conditions:

Initial conditions were applied uniformly over the model geometry and are described in Table 4.

Table 4: Initial conditions for the 2-D and 3-D models.

Temperature	Pressure	Displacement Field	Velocity Field
25 °C	1 atm	0 m	0 m/s

There were three boundary conditions applied: HIP pressure load, pore pressure load, and symmetric constraint. The HIP pressure load was applied to the exterior surface of the solid volume and varied with time according to the HIP cycle pressure level shown in Figure 11 for the baseline case. The symmetric constraint is applied to four symmetric boundaries intersecting the solid volume, and the pore pressure load is applied to the pore wall. The symmetric constraint restricts motion in the direction normal to the symmetric boundaries as per Equation 12. Although the model geometry could be divided into quarter symmetric volumes, in order to assess the effect of stress distribution away from the pore when varying representative modeling volume the full 2-D model was preserved. The pore pressure load is calculated as a ratio of initial and current pore volume to provide a current gas density and follows the ideal gas law as shown in Equation 13. Surfaces on the 2-D model where boundary conditions are applied are shown in Figure 4.

Equation 12: Symmetric constraint equation.

$$u \cdot n_s = 0$$

Equation 13: Pore pressure load calculation.

$$P_{pore} = \left(\frac{V_{0\,pore}}{V_{pore}} \rho_{Ar} \right) \frac{RT}{M_{Ar}}$$
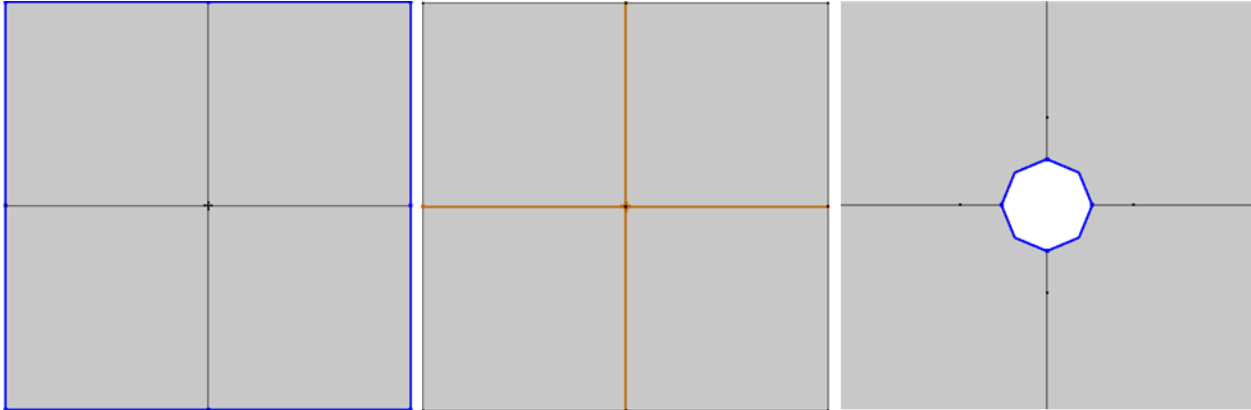
Figure 4: 2-D model boundary condition surfaces. HIP pressure load surface in blue (left), symmetric constrained surfaces in brown (center), and the pore pressure load surface in blue (right).

The HIP pressure and pore pressure boundary loads are implemented in the structural model as shown in Equation 14. Here the boundary load vector F_A acts as a distributed load on the reference surface normal n_0 and is translated to the spatial frame via the deformation gradient tensor F.

Equation 14: Boundary load implementation.

$$F_A = S \cdot n_s$$

Solver settings:

A transient multi-physics formulation was used for this analysis. Quadratic serendipity shape functions were used as the default discretization throughout the model. The equations developed in the finite element model were combined into a fully coupled system and the resulting non-linear problem was solved iteratively using a damped version of Newton's method and a direct linear systems solver (MUMPS). The non-linear solver was permitted to automatically choose a damping factor in each iteration of Newton's method with the following specifications: the initial damping factor was 1, the minimum damping factor permitted was 0.5, and the damping factor change in between iterations was restricted to a maximum of 10. Further, if the solver gets stuck at the minimum damping factor, a constant damping factor of 0.75 was specified which the solver will initiate in attempts to recover. As the solver iterated, a solution-based estimate of the relative error was calculated. When this relative error estimate became smaller than 0.01, or 4 iterations were completed, the solver terminated and proceeded to the next time step in the transient analysis. The direct solver for the linear system of equations used was MUMPS. Transient solver time steps were calculated using a backward differentiation formula (BDF). The solver was forced to take time steps at specified times – especially important were times which aligned with changes in the HIP cycle pressure or temperature such as commencement of ramps – but free to determine steps at non-specified times. The maximum allowable time step was 200 s; this maximum step was determined to be useful in preventing the solver from taking much larger timesteps at certain points in the HIP cycle which resulted in the accumulation of error and ultimately divergence of the solution. The maximum allowed degree of the interpolating polynomial of the BDF method was 5 and the minimum was 1.

3.2 3-D Spherical Model Description

A 3-D spherical pore model was developed and run in a single case in order to provide a comparison to the 2-D model baseline case. The 3-D spherical model implementation was the same as in the 2-D model, except for a few key differences. A full view of the 3-D spherical pore model showing elements in visible in Figure 5.
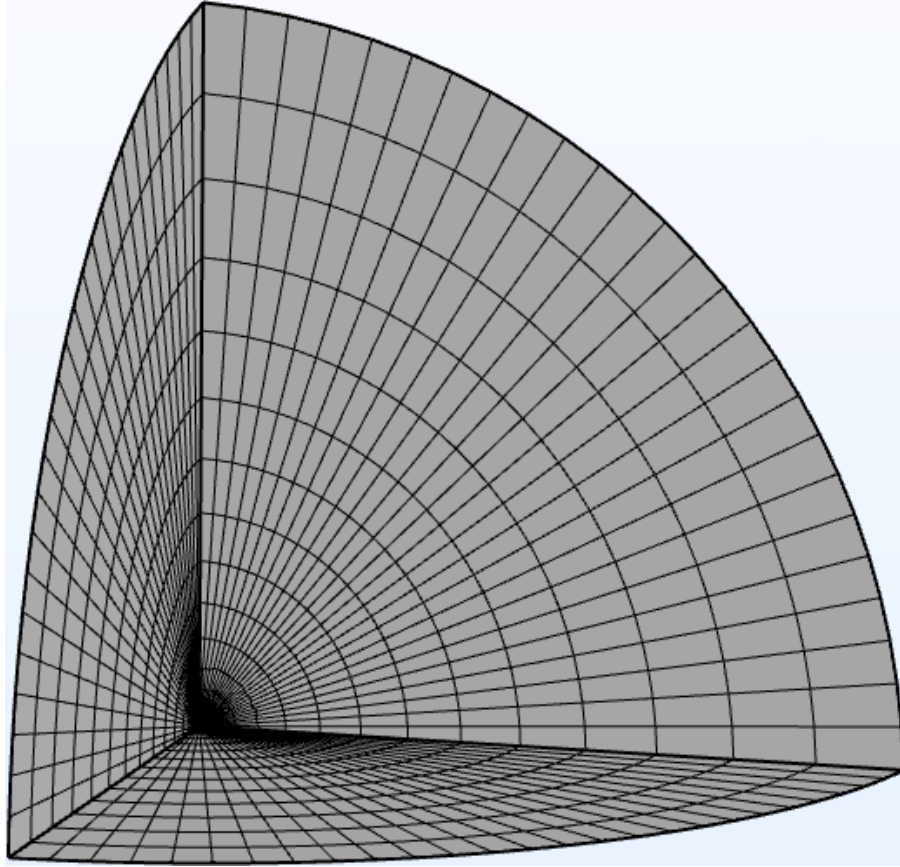
Figure 5: View of the full meshed 3-D spherical pore model geometry. The relatively tiny central pore is not visible at this scale.

In contrast to the 2-D model, which has square external boundaries, the external boundaries of the 3-D spherical pore model are spherical. Further, the 3-D model is a $1/8^{th}$ model reduced about the x, y, and z planar symmetric boundaries. Views of the 3-D spherical pore model mesh that are zoomed in to show mesh region interfaces are seen in Figure 6. Because the external volume and pore boundaries are spherical there is no transition in the shape of the radial mesh divisions as exists in the 2-D model, which has a square external boundary. The mesh count variable used to construct the 3-D model mesh was reduced from the 2-D baseline case in order to accommodate the significant increase in computational cost resulting from the 3-D geometry. 3-D model parameter settings are shown in Table 12.
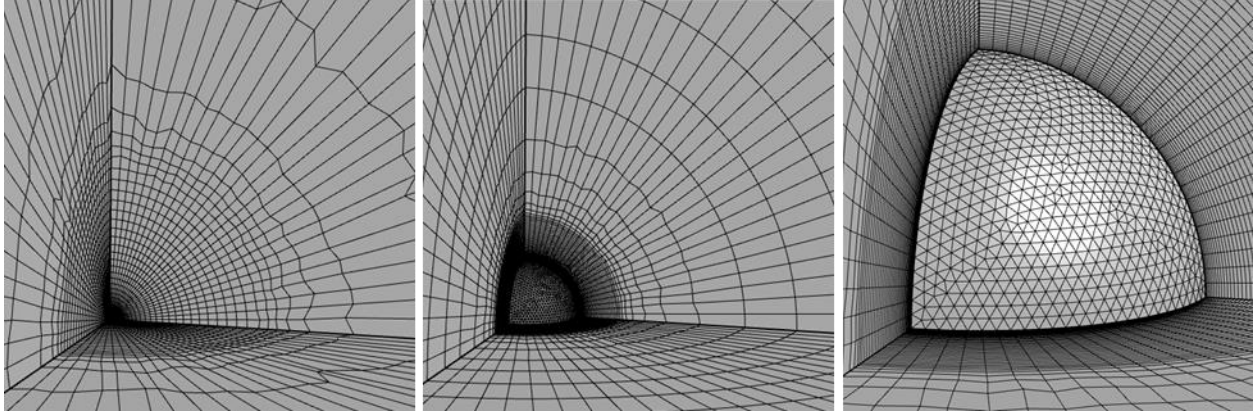
Figure 6: 3-D spherical pore model mesh regions. Showing interface between low and medium density (left), medium and high (center), and the pore wall (right).

The three boundary conditions were applied as with the 2-D model: HIP pressure load, pore pressure load, and symmetric constraint. The pore pressure load calculation is unchanged from the 2-D model except that the pore volume is calculated for a sphere rather than a cylinder. The symmetric constraint is applied to the three external boundaries which result from the $1/8^{th}$ model reduction about the x, y, and z symmetric planes. Surfaces on the 3-D spherical pore model where boundary conditions are applied are shown in Figure 7.
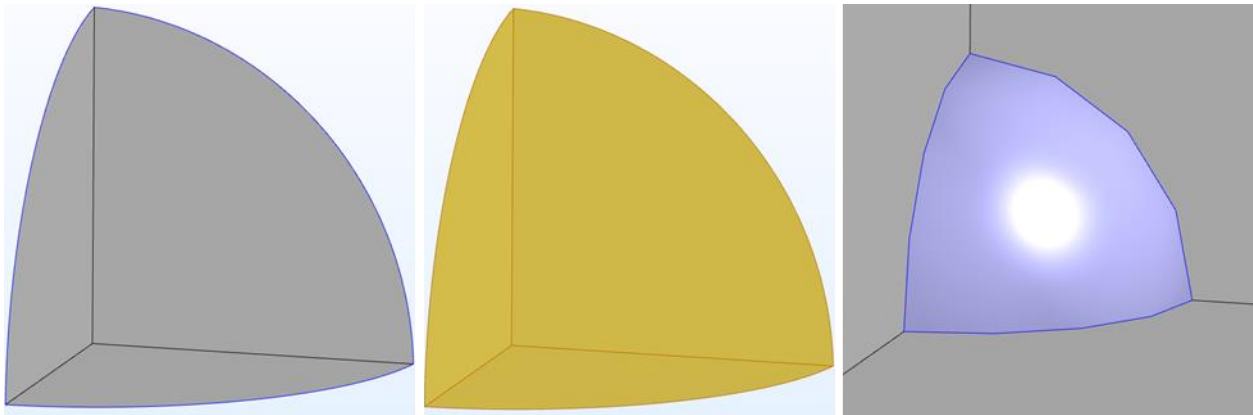
Figure 7: 3-D spherical pore model boundary condition surfaces. HIP pressure load surface in blue outline (left), symmetric constrained surfaces in brown (center), and the pore pressure load surface zoomed in blue (right).

The physics employed in the 3-D model were the same as in the 2-D model except that the plane strain assumption was not applied.

3.3 Assumptions

In order to provide predictions within the limit of computational resources and schedule, several modeling assumptions were necessary. These assumptions are now summarized.

Assumptions related to geometry and symmetry:

1. The pore, and surrounding solid volume, is assumed to be symmetric. The primary reason for this assumption is the lack of pre-HIP pore geometry data due to restricted laboratory access. Samples originally intended to be analyzed in this study contain seeded spherical and cylindrical defects. Consequently, 2-D round (pseudo-cylindrical) and 3-D spherical perfectly symmetric pores were modeled. Predictions under this assumption can be considered a simplified representation of the expected deformation process; however, as it has not been possible to experimentally investigate initial and final pore shape and size, the assumption greatly simplified model geometry and meshing. It should be noted, full pore closure was not possible to model due to the symmetry of the pore throughout the HIP cycle.
2. Due to inherent model symmetry, a symmetric boundary condition was selected. Symmetric planes were selected within the model and displacement in the normal direction at these planes was constrained. In the case of the 2-D model, these planes were lines which intersected the center of the pore along the x and y axes; in the case of the 3-D model, 2-D planes were selected which intersect the center of the pore along the x, y, and z axes. The 3-D model was reduced to 1/8 its original size by segmenting the full geometry about these planes and deleting all but one remaining section; consequently, the symmetric boundary conditions are applied to external boundaries in the 3-D model. The symmetric boundary condition restrains displacement normal to the boundary.
3. Primarily, analysis was conducted on a 2-D model with a select run for comparison using a 3-D model reduced in size about symmetric axes. This assumption is primarily to reduce computational load and accelerate solution times and is reasonable due to the symmetry of the pore and representative volume geometry and boundary conditions. Considering schedule limitations, the 2-D model provided the opportunity to investigate general trends, outlined in this report, but not predict specific empirical pore geometries which include out of plane effects.
4. Location of the pore within the part, including proximity to load surfaces, and the effect of neighboring defects was ignored. A representative volume of homogenous isotropic solid material was assumed to surround the single pore in the model. The size of the representative volume selected was large enough to not influence pore closure. As it was necessary to model a single pore, the most generalizable predictions were made by assuming a large solid volume surrounding the pore; however, in reality neighboring defects and variations in the local stress field due to location within the part would affect pore closure in a unique way for each pore.

5. In the 2-D model, the pore modeled is a round hole in a flat plane. For purposes of calculating pore pressure and pore volume, a cylindrical shape is assumed, and cylinder height is not defined. Not defining cylinder height necessitates the assumption that initial and final height do not change throughout the HIP cycle. This assumption effects pore closure and pressure calculations in the 2-D case only, and is necessary as out of plain strains, and by extension deformation, are not a part of the 2-D model definition.
6. 2-D model plain strain assumption where all out-of-plane strain components are null and there is no variation of in-plane strain components in the normal direction.

Assumptions related to solid (substrate) material properties:

1. Solid material properties are assumed to be homogenous and isotropic; crystal plasticity, boundary diffusion, and other microstructural effects are not considered. The effects of microstructure on deformation will be more significant for smaller pores as the size of the microstructural features relative to the pore become more equivalent. This assumption was necessary given the short duration of the model development schedule.
2. Solid material properties were used as available in literature and likely do not reflect the behavior of microstructure characteristic in as-built samples. As-built microstructures are generally highly anisotropic, with features characteristic of the high temperature and high cooling rate of the additive process and contain a number of defects of various sizes and shapes. Further, Inconel material properties are affected by the time-temperature-precipitation of various intermetallic phases which would be unique to the additive process and process parameters used to fabricate a specific sample. The effect of these precipitates and microstructural features would best reflect the material properties of the samples tested for data gathered from literature. As-built material properties are available in literature (Project 4026: Development of Distortion Prediction and Compensation Methods for Metal Powder Bed Fusion Additive Manufacturing 2018); however, these properties were not used as they are process dependent and would reflect the effect of defects rather than the bulk solid properties required for the modeling of a single pore surrounded by a representative volume of solid material.
3. Most elastic material properties reported in literature were calculated using other measured properties. Specifically, density was calculated using mean measured coefficient of thermal expansion and Poisson's ratio was calculated from measured Young's modulus and torsional modulus data.

Assumptions related to pore material properties:

1. Pore internal gas is assumed pure argon with initial pressure equivalent to 1 atm. Argon is a common powder bed metallic additive manufacturing machine cabin gas. This assumption neglects the effects of metal vapor on any pores formed. Metal vapor will displace cabin gas and condense resulting in reduced pore gas pressure. This assumption would result in predictions that are more accurate for "lack of fusion" type pores and less accurate for "keyhole" type pores.
2. Ideal gas law is used to calculate pore internal argon gas pressure. At high temperatures and pressures, such as the HIP cycle hold temperature and pressure, the ideal gas law may have reduced accuracy.

Assumptions related to physics models:

1. HIP process temperature cycle was applied uniformly to the model volume; heat diffusion was not considered. In reality, heat energy would take some time to transmit from the part boundary inward; however, given the part size and HIP cycle hold times this assumption will have minimal impact on the accuracy the predicted deformation.
2. The ramp rates for the HIP process temperature and pressure cycle were assumed. The project provided hold pressure, hold temperature, and hold time only. Consequently, rates were assumed based on (Tillmann, et al. 2017). These rates have minimal impact on pore closure, but there is some effect resulting from creep when temperatures are high.
3. Heat generation caused by deformation is considered negligible and therefore ignored.
4. Diffusion of argon gas across the pore wall into the substrate was ignored.
5. Contact between pore wall boundaries was ignored. Further description is included in the future work section below.
6. Material models selected were by default assumptions and each model incorporated additional assumptions into the overall approach:
    a. Elasticity: A linear elastic model was selected due to the relative simplicity of the model and the small elastic contribution to strain during the HIP cycle. Inelastic strain components, specifically plasticity and creep, were incorporated into the linear elastic model using a large plastic strains assumption whereby deformation gradient tensor components were decomposed by multiplication.
    b. Plasticity: The Johnson-Cook material model was selected for this analysis primarily due to the wide-spread use of the model and consequent availability of model parameters for several materials including IN718. Johnson-Cook is an isotropic strain and strain rate hardening model, and this approach incorporated a thermal softening term. Material model parameters used in this analysis were taken from (Iturbe, et al. 2017) where they were generated using uniaxial compression test data for temperatures in the range 21–1050 °C and strain rates $1 - 100$ s-1 of IN718 specimen. The traditional Johnson-Cook strain and strain rate hardening terms were used from the paper, but the thermal softening function used was a form developed by the authors. Von Mises stress criterion was used in the yield stress calculations.
    c. Creep: Norton power law creep was implemented for this analysis primarily due to the simplicity and wide-spread use of the model and the availability of model parameters for IN718. Identifying model parameters for temperature and strain conditions relevant to this study proved difficult, and ultimately parameters were generated by fitting the Norton power law function form to published test data found in (Chavez, et al. 1994). This is described in the discussion section. An Arrhenius type temperature term was employed; the activation energy used in that term was taken from (Chaturvedi and Han 1989). Chaturvedi, et. al. described the significant effects that grain structure has on creep deformation of IN718; consequently, the grain structure of the specimen used in the Chavez, et. al. data, a consequence of test specimen heat treatment, was an assumption of consequence to the creep model.

7. Surface tension effects were ignored. Surface tension effects cause irregular pores to assume more spherical shapes during deformation and dominate pore closure when defects fall below a certain size known as the critical pore size. These effects are described in (Atkinson and Davies 2000). The critical pore diameter for IN718 is estimated at 38.8 nm using calculations from an approach published in (Epishin, et al. 2018). Surface tension is safely ignored in this analysis both because final pore closure was always much larger than the calculated critical pore size and pores were always assumed symmetric.
8. Transient simulation assumes a quasi-static approach; second order time derivatives are assumed null. This assumption simplifies the model solution and is appropriate due to the relatively slow changes in HIP cycle temperature and pressure with respect to time.

3.4 Material Properties

Elastic material properties:

Temperature dependent elastic material properties were estimated from polynomial fit equations of referenced data. These fit equations are provided in the COMSOL Multiphysics® Material Library which is an add-on to the basic software package. The data sources referenced by COMSOL Multiphysics® for the development of the fit equations are (Special Metals Corporation 2007) and (United States Department of Defense 1998). The fit equations, bounds, and plots are shown below. In each plot, the property is shown for the full range of temperature over the HIP cycle for the baseline case from ambient to hold. Dashed lines are shown where the HIP cycle temperature exceeded the bounds of the fit equations and the final value was extrapolated and used for the analysis.

The fit for density is provided in Equation 15. The fit provides density in kg/m^3 as a function of temperature in units of K and is valid between 33 K and 1144 K. Figure 8 shows a plot of the fit equation over the range of baseline HIP temperatures. IN718 density was calculated from measured linear coefficient of thermal expansion data reported in the references.

Equation 15: Density material property fit equation.

$$\rho =$$
$$8288.965 - 0.05548692T - 7.190094e^{-4}T^2 + 7.974854e^{-7}T^3 - 3.478001e^{-10}T^4$$
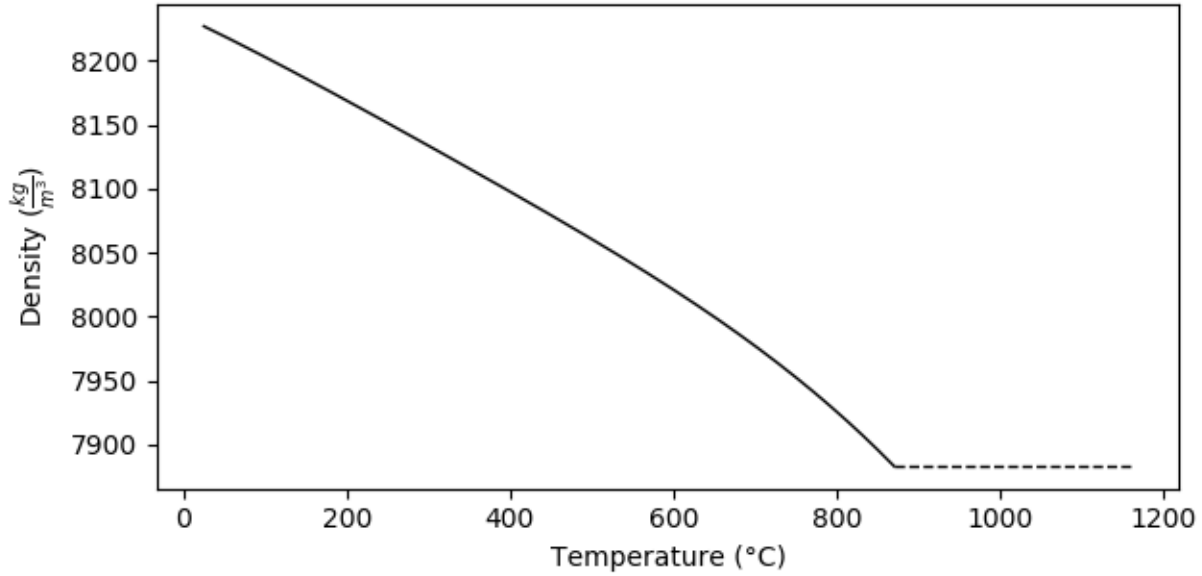
Figure 8: Density for IN718 used in the elastic material model over the range of baseline HIP temperatures for this analysis. Dashed lines indicate extrapolated values.

The fit for the modulus of elasticity in tension is provided in Equation 16. The fit provides modulus values in units of Pa as a function of temperature in units of K and is valid between 200 K and 1366 K (1093 °C). Figure 9 shows a plot of the fit equation over the range of baseline HIP temperatures. Specimen used to produce data for the modulus of elasticity in tension were hot-rolled flat and heat-treated. Heat treatment regimen was 1800 °F (982 °C)/1 hour air cool, plus 1325 °F (718 °C)/8 hours furnace cool, plus 20 °F (11.1 °C)/hour ramp to 1150 °F (621 °C) and held for total aging time of 18 hours.

Equation 16: Modulus of elasticity in tension material property fit equation.

$$E = 2.216171e^{11} - 1.071145e^{8}T + 118609.2T^2 - 77.87834T^3$$
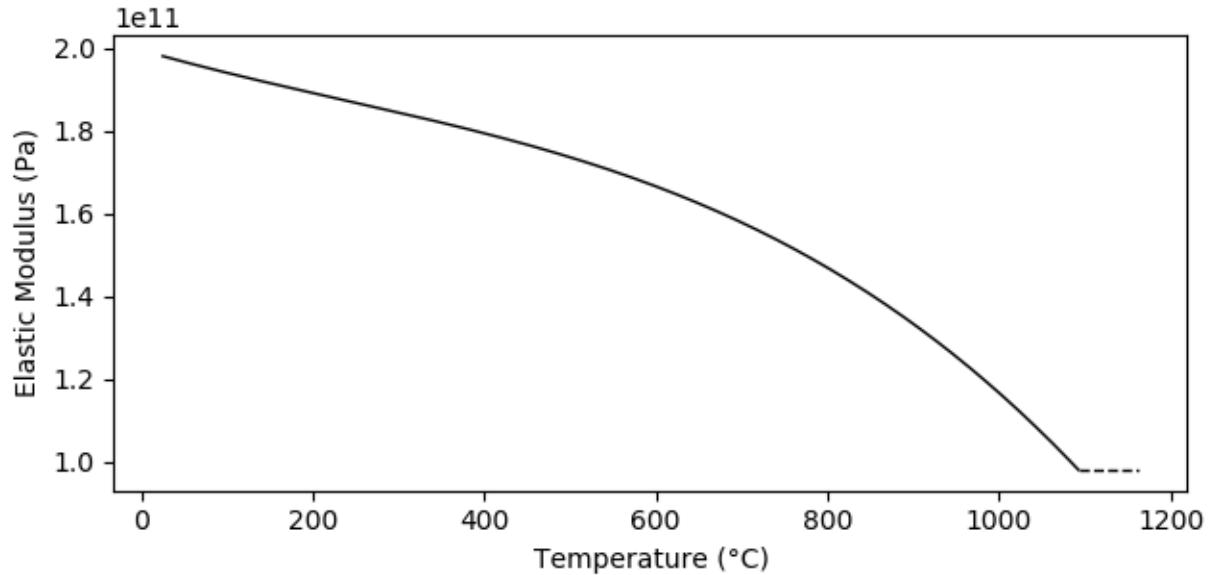
Figure 9: Elastic modulus for IN718 used in the elastic material model over the range of baseline HIP temperatures for this analysis. Dashed lines indicate extrapolated values.

The fit for Poisson's ratio is provided in Equation 17. The two-part piecewise fit provides non-dimensional values as a function of temperature in units K and is valid between 200 K (-73 ºC) and 1366 K. Figure 10 shows a plot of the fit equation over the range of baseline HIP temperatures. IN718 Poisson's ratio was calculated from measured elastic modulus in tension (E) and elastic modulus in shear data reported in the references by assuming isotropic behavior.

Equation 17: Poisson's ratio material property fit equation.

$$\nu =$$

$$\begin{cases} 0.3046558 - 9.703382E - 5T^1 + 7.919159E - 8T^2; \ 200 \le T \le 800 \ K \\ -0.3168756 + 0.001877752T^1 - 2.021026E - 6T^2 + 7.534566E - 10T^3; \ 800 \le T \le 1366 \ K \end{cases}$$
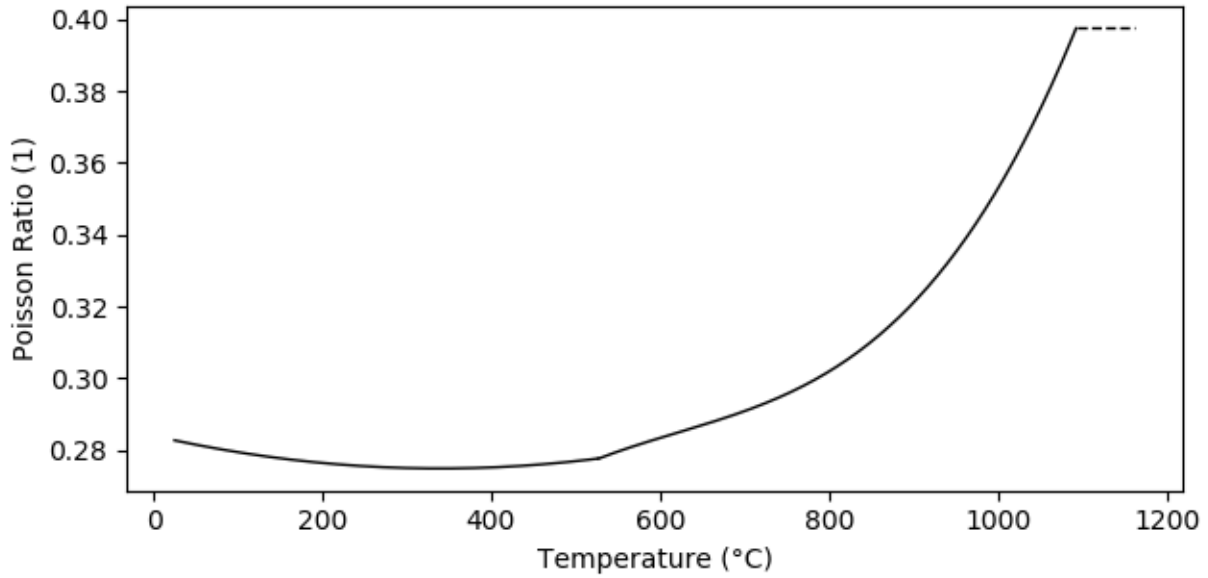
Figure 10: Poisson ratio for IN718 used in the elastic material model over the range of baseline HIP temperatures for this analysis. Dashed lines indicate extrapolated values.

Pore gas properties:

Widely available properties for Argon gas were used to compute the gas pore pressure as a function of pore closure. The following properties were assumed:

Equation 18: Argon gas properties.

$$M_{Ar} = 39.948 \ \frac{g}{mol}$$

$$\rho_{Ar} = \ 1.784 \ \frac{kg}{m^3}$$

4.0 METHODS

Primary model analysis was conducted on the 2-D model. Select 3-D cases were run and are clearly indicated as such during discussion. Model performance and quality checks were performed by analyzing results over several parametric studies where five parameters were held constant as controls and a sixth was varied. The six parameters involved in these studies were representative volume length, pore diameter, mesh count, HIP hold pressure, HIP hold temperature, and HIP hold time. A baseline case was selected for comparison. The baseline values for HIP hold pressure, HIP hold temperature, and HIP hold time were provided by the project. This baseline case is described in Table 5.

Table 5: Baseline case parameters

Representative Volume Length (m)	Initial Pore Diameter (µm)	Mesh Count	HIP Hold Pressure (MPa)	HIP Hold Temperature (°C)	HIP Hold Time (h)
.5	100	70	103	1163	4

Representative volume length describes the length of one side of the square 2-D plane surrounding the pore. The purpose of this parametric study is to ensure that the representative volume selected for analysis is sufficiently large such that varying its size does not affect the predicted pore closure resulting from deformation of the solid volume. In order to ensure that the representative volume selected was large enough to be held constant while varying the initial pore diameter parameter (see Table 7), the largest pore diameter in the study – 800 µm – was selected as the control value for pore diameter in this representative volume length study. The other parameters for this study were held at baseline settings. The parametric case settings for the representative volume length study are shown in Table 6.

Table 6: Varying representative volume length

Case	Representative Volume Length (m)	Initial Pore Diameter (µm)	Mesh Count	HIP Hold Pressure (MPa)	HIP Hold Temperature (°C)	HIP Hold Time (h)
1-1	.5	800	70	103	1163	4
1-2	.1	800	70	103	1163	4
1-3	.05	800	70	103	1163	4
1-4	.025	800	70	103	1163	4
1-5	.01	800	70	103	1163	4

Pore diameter describes the initial diameter of the round symmetric pore. The purpose of this study is to show how the final pore size after the full HIP cycle has completed varies with initial pore diameter. The other parameters for this study were held at baseline settings. The parametric case settings for the pore diameter study are shown in Table 7.

Table 7: Varying initial pore diameter

Case	Representative Volume Length (m)	Initial Pore Diameter (µm)	Mesh Count	HIP Hold Pressure (MPa)	HIP Hold Temperature (°C)	HIP Hold Time (h)
2-1	.5	800	70	103	1163	4
2-2	.5	400	70	103	1163	4
2-3	.5	100	70	103	1163	4
2-4	.5	50	70	103	1163	4
2-5	.5	25	70	103	1163	4
2-6	.5	10	70	103	1163	4
2-7	.5	5	70	103	1163	4

Mesh count describes a scalar that is used throughout the mesh build to determine overall mesh density and is described in detail in the model description section. The purpose of this study is to see that the selected mesh count is large enough to ensure independence of the mesh density and predicted pore closure resulting from deformation of the solid volume. In order to ensure that the mesh count selected was large enough to be held constant while varying the initial pore diameter parameter (see Table 7), the smallest pore diameter in the study – 5 µm – was selected as the control value for pore diameter in this mesh count study. The reason for this is that the smallest pore diameter, given the same baseline representative volume length (.5 µm), would produce the largest region of solid material to mesh in the pore diameter study test matrix; the result would be the lowest mesh density and therefore the most challenging to resolve computationally. The other parameters for this study were held at baseline settings. The parametric case settings for the mesh count study are shown in Table 8.

Table 8: Varying mesh count

Case	Representative Volume Length (m)	Initial Pore Diameter (µm)	Mesh Count	HIP Hold Pressure (MPa)	HIP Hold Temperature (°C)	HIP Hold Time (h)
3-1	.5	5	70	103	1163	4
3-2	.5	5	60	103	1163	4

3-3	.5	5	50	103	1163	4
3-4	.5	5	40	103	1163	4
3-5	.5	5	30	103	1163	4
3-6	.5	5	20	103	1163	4
3- 7	.5	5	15	103	1163	4
3- 8	.5	5	10	103	1163	4

HIP hold pressure describes the external boundary pressure applied to the model during the hold phase of the HIP cycle. The purpose of this study is to assess the effect of varying HIP hold pressure on the predicted pore closure resulting from deformation of the solid volume. The HIP hold pressure was varied +/- 10% of the baseline value. The other parameters for this study were held at baseline settings. The parametric case settings for the HIP hold pressure study are shown in Table 9.

Table 9: Varying HIP hold pressure

Case	Representative Volume Length (m)	Initial Pore Diameter (μm)	Mesh Count	HIP Hold Pressure (MPa)	HIP Hold Temperature (°C)	HIP Hold Time (h)
4-1	.5	100	70	92.7	1163	4
4-2	.5	100	70	103.0	1163	4
4-3	.5	100	70	113.3	1163	4

HIP hold temperature describes the uniform temperature applied to the model during the hold phase of the HIP cycle. The purpose of this study is to assess the effect of varying HIP hold temperature on the predicted pore closure resulting from deformation of the solid volume. The HIP hold temperature was varied -10%, -5%, 0%, and +5% of the baseline value. The other parameters for this study were held at baseline settings. Pore closure was most sensitive to HIP hold temperature relative to pressure and hold time; consequently, four temperature settings were analyzed rather than three settings in the pressure and hold time studies. Further there was a bias toward lower temperatures relative to baseline; this is because deformation rates became high enough to cause solver convergence issues above +5% of baseline temperature. The parametric case settings for the HIP hold temperature study are shown in Table 10.

Table 10: Varying HIP hold temperature

Case	Representative Volume Length (m)	Initial Pore Diameter (μm)	Mesh Count	HIP Hold Pressure (MPa)	HIP Hold Temperature (°C)	HIP Hold Time (h)
5-1	.5	100	70	103	1046.7	4
5-2	.5	100	70	103	1104.9	4
5-3	.5	100	70	103	1163.0	4
5-4	.5	100	70	103	1221.2	4

HIP hold time describes the duration of the hold phase of the HIP cycle when HIP hold temperature and pressure are applied to the model. The purpose of this study is to assess the effect of varying HIP hold time on the predicted pore closure resulting from deformation of the solid volume. The HIP hold time was varied according to suggested inputs from the project. The other parameters for this study were held at baseline settings. The parametric case settings for the HIP hold time study are shown in Table 11.

Table 11: Varying HIP hold time

Case	Representative Volume Length (m)	Initial Pore Diameter (μm)	Mesh Count	HIP Hold Pressure (MPa)	HIP Hold Temperature (°C)	HIP Hold Time (h)
6-1	.5	100	70	103	1163	.5
6-2	.5	100	70	103	1163	4
6-3	.5	100	70	103	1163	8

A 3-D spherical model was run as a single case primarily for comparison to the baseline 2-D (pseudo cylindrical) model case in order to assess the effects of geometry. The 3-D model follows the baseline conditions, shown in Table 12, as close as possible with the exception of mesh count which was reduced in order to facilitate the considerable increase in computational load with the 3-D model. Here the representative volume length specified the diameter of the solid volume sphere rather than the length of the square as in the 2-D model.

Table 12: 3-D spherical model conditions

Representative Volume Length (m)	Initial Pore Diameter (μm)	Mesh Count	HIP Hold Pressure (MPa)	HIP Hold Temperature (°C)	HIP Hold Time (h)
.5	100	40	103	1163	4

5.0 RESULTS

Baseline case conditions are outlined in Table 5, and the results are useful as a reference for other cases. The HIP cycle conditions – HIP hold pressure, HIP hold temperature, and HIP hold time – effect the loading and material response of the solid material. Pressure and temperature ramp rates and ramp initiation timing were assumed based on published values (Tillmann, et al. 2017). These values specify a temperature ramp over 90 minutes followed by a pressure ramp rate of 5 MPa/min from ambient to the beginning of the hold. At the conclusion of the hold, both the temperature and pressure ramps back to ambient are initiated simultaneously and occurred at the same but reversed rates as the initial ramps to the hold conditions. The full temperature and pressure HIP cycle over time is shown graphically in Figure 11. This HIP cycle was used for all cases except in the HIP hold pressure, HIP hold temperature, and HIP hold time parametric studies.
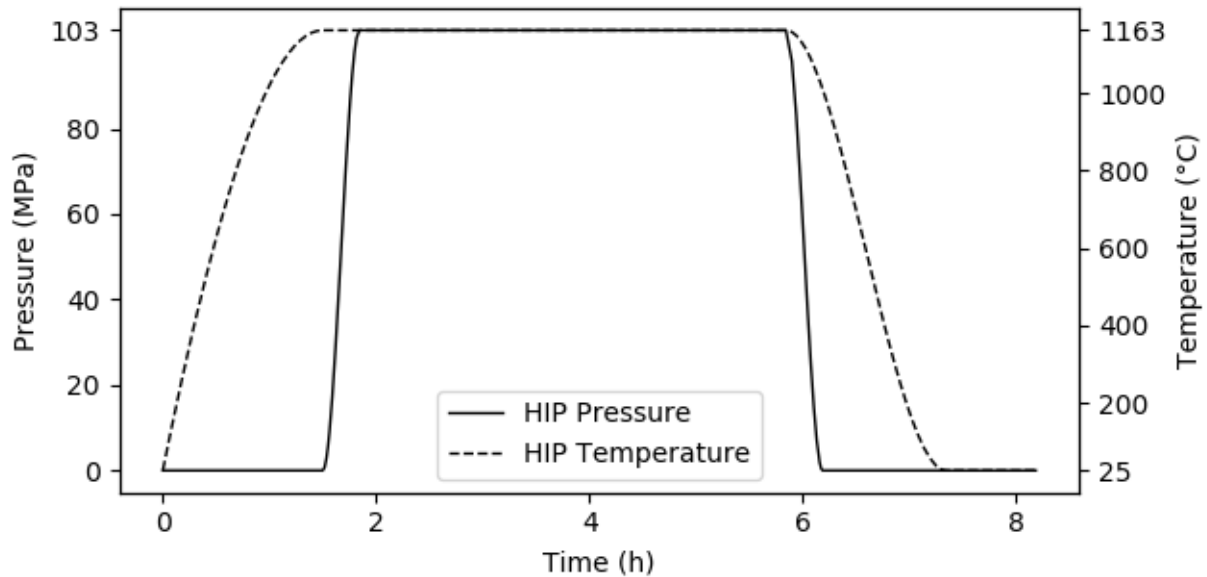
Figure 11: Baseline HIP cycle showing temperature and pressure ramps and hold.

The primary model prediction of interest is pore closure. Pore closure is reported in two ways: pore volume closure percentage and pore diameter. Pore volume closure percentage indicates the percentage of full closure by volume with 0.0% corresponding to the initial volume (no closure) and 100.0% with full closure at an internal pore volume of 0.0 m^3. A negative value would indicate that the pore had expanded relative to the initial volume. Pore volume closure percentage is a relative indicator of closure and is calculated as in Equation 19.

Equation 19: Pore volume closure percentage

$$pore\ volume\ closure\ percentage = \left(1 - \left(\frac{V_{pore}}{V_{0\,pore}}\right)\right)100$$

Pore diameter, which is the diameter at the conclusion of the HIP cycle, is an absolute value and depends on initial pore diameter, which is 100 μm for the baseline case. The results of pore closure, showing both pore volume closure percentage and pore diameter are shown for the baseline case in Figure 12. At the baseline conditions, the initial 100 μm pore was reduce by 24 μm to 76 μm, and pore volume closure was reduced to 42.8% of full closure. Note the pore was still deforming when the hold concluded. Consequently, for baseline conditions pore closure was limited by hold time rather than pore pressure or closure. The cycle commences with only the HIP temperature ramp. As the HIP temperature increases, gas pore pressure increases which causes a slight expansion of the pore under no external pressure loading. The maximum pore increase is about 0.0012% by volume or an increase in diameter of about 0.0006 μm. After HIP temperature has stabilized at the baseline hold setting, the pressure ramp commences, and the pore begins to contract. Pressure stabilizes and the hold commences. At the conclusion of the hold, the pore is at its minimum size of 75.64 μm or 42.78% of full closure. The pressure and temperature ramps back to ambient commence simultaneously; however, the temperature ramp is slower which allows some plastic deformation in the direction of pore expansion due to high pore gas pressure in addition to the elastic relaxion with the removal of the pressure load. This pore re-expansion, an increase in diameter of 0.10 μm or 0.14% by volume, results in a final pore diameter of 75.74 μm or 42.64% of full closure by volume. It is then clear that pore expansion occurs predominantly during the post HIP cycle ramp rather than the pre-HIP cycle ramp.
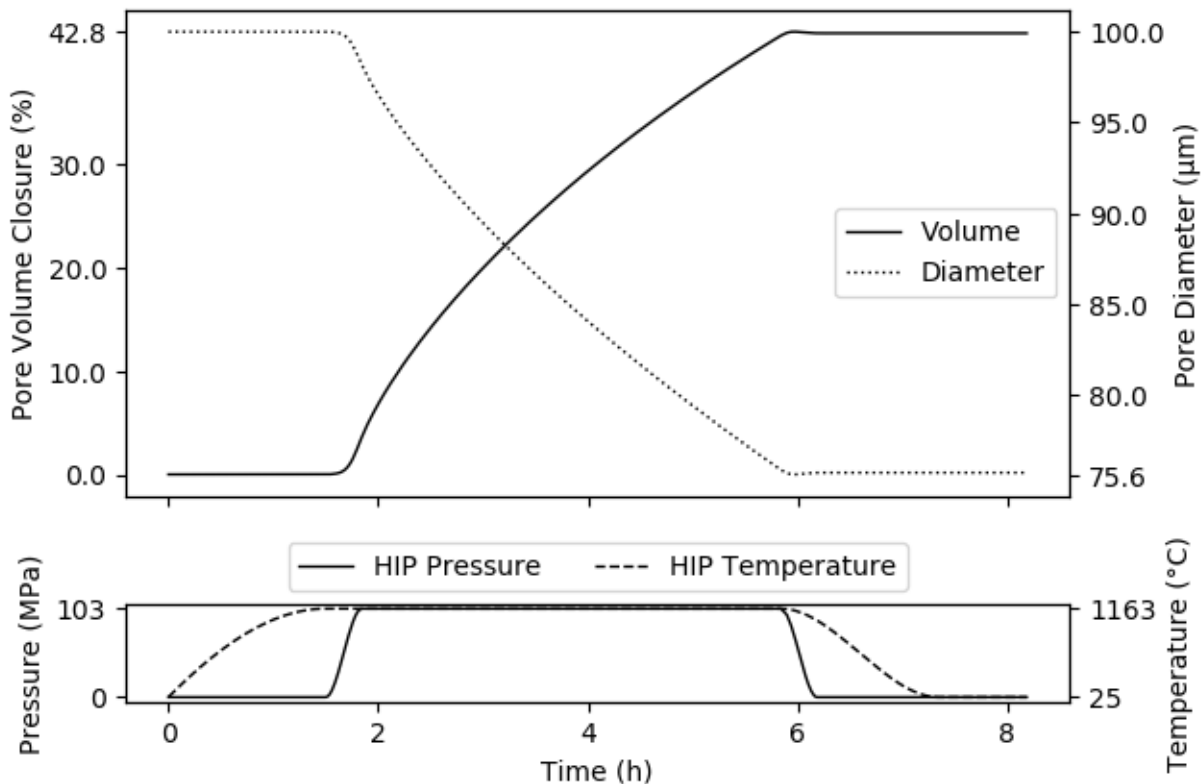
Figure 12: Baseline case pore closure.

Pore pressure indicates the pore internal gas pressure due to changes in volume and temperature over the HIP cycle. Pore pressure for the baseline case is shown in Figure 13. The initial pore pressure is 0.0 MPa over ambient and is in equilibrium with the external pore pressure. It should be noted that the initial pressure used in pore gas material properties calculations is 1 atm; consequently, pore pressure reflects the pressure change relative to ambient. As pore pressure increases, a load is applied normal to the pore walls which acts to slow further collapse. At baseline conditions, pore pressure initially rises due to increasing HIP temperature prior to the application of HIP pressure. This initial increase in temperature driven pore pressure results in an expansion of the pore volume by 0.0012% or an increase in diameter of about 0.0006 μm. After HIP temperature stabilizes, and before HIP pressure is applied, pore gas pressure stabilizes briefly; after, pore closure resulting from solid material deformation during the pressure ramp and hold results in a stable increase in internal pore pressure. The rate of increase in pore pressure is initially nonlinear during the pressure ramp but becomes linear during the hold. At the end of the hold, HIP pressure and temperature both ramp down simultaneously resulting in a sharp decrease in pore pressure. This decrease is due to both the decrease in temperature as well as an increase in pore volume resulting from elastic strain relaxation – apparent in Figure 15 – and some creep and plastic deformation which occurs after the more rapid pressure ramp has completed but the slower temperature ramp is still underway. After the conclusion of the HIP cycle, temperature has returned to ambient and the partially closed pore volume is stable; the final pore pressure for the baseline case is 0.08 MPa over ambient.
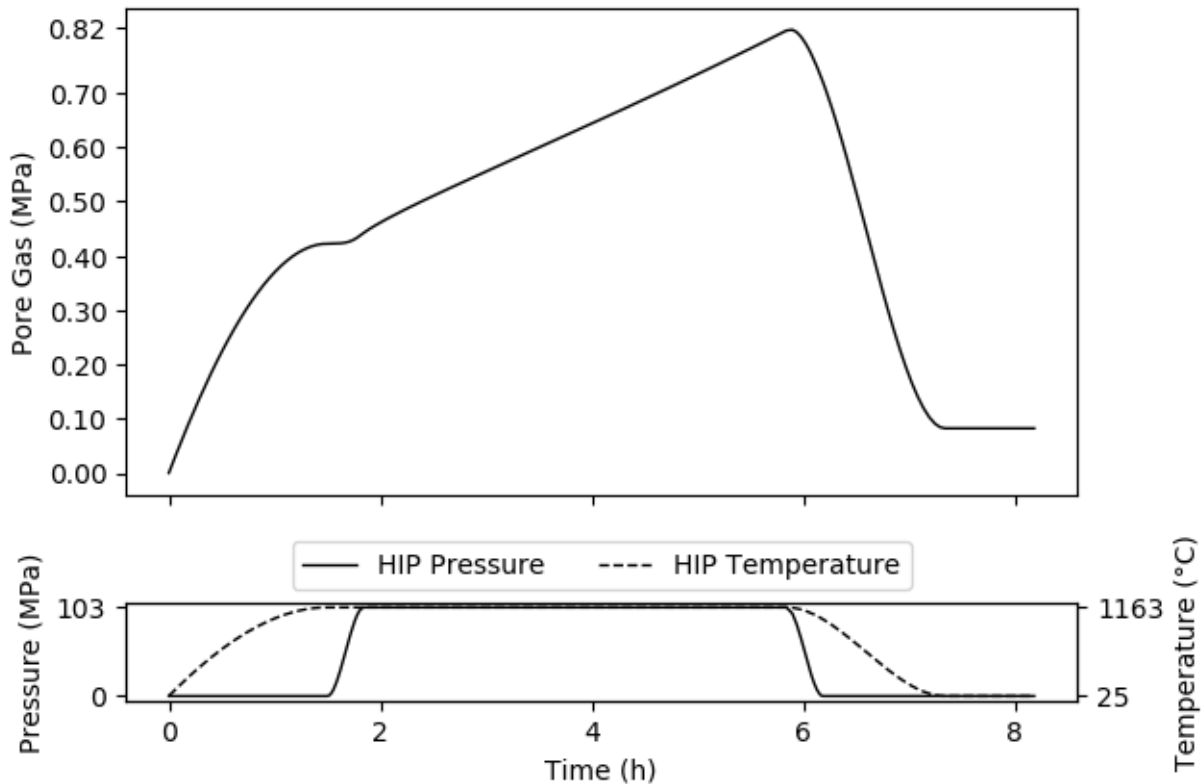
Figure 13: Baseline case pore gas pressure. Final pressure after completion of HIP cycle is 0.08 (MPa).

Figure 14 shows total strain normal to the pore wall surface and the relative contribution of elastic, plastic, and creep components to the total strain. Clearly, strain is dominated by creep in the baseline case. This is true for all cases simulated for this effort. In the baseline case, creep accounts for 87.7% of the total strain at the conclusion of the HIP cycle. Consequently, one key finding from this effort is the importance of an accurate creep material model and model parameters. Due to time and center access limitations, material models and their parameters were estimated using data from literature and are likely limited in their ability to accurately predict the material response of the specific alloy to relevant conditions. This is discussed in greater detail in another section of this report.
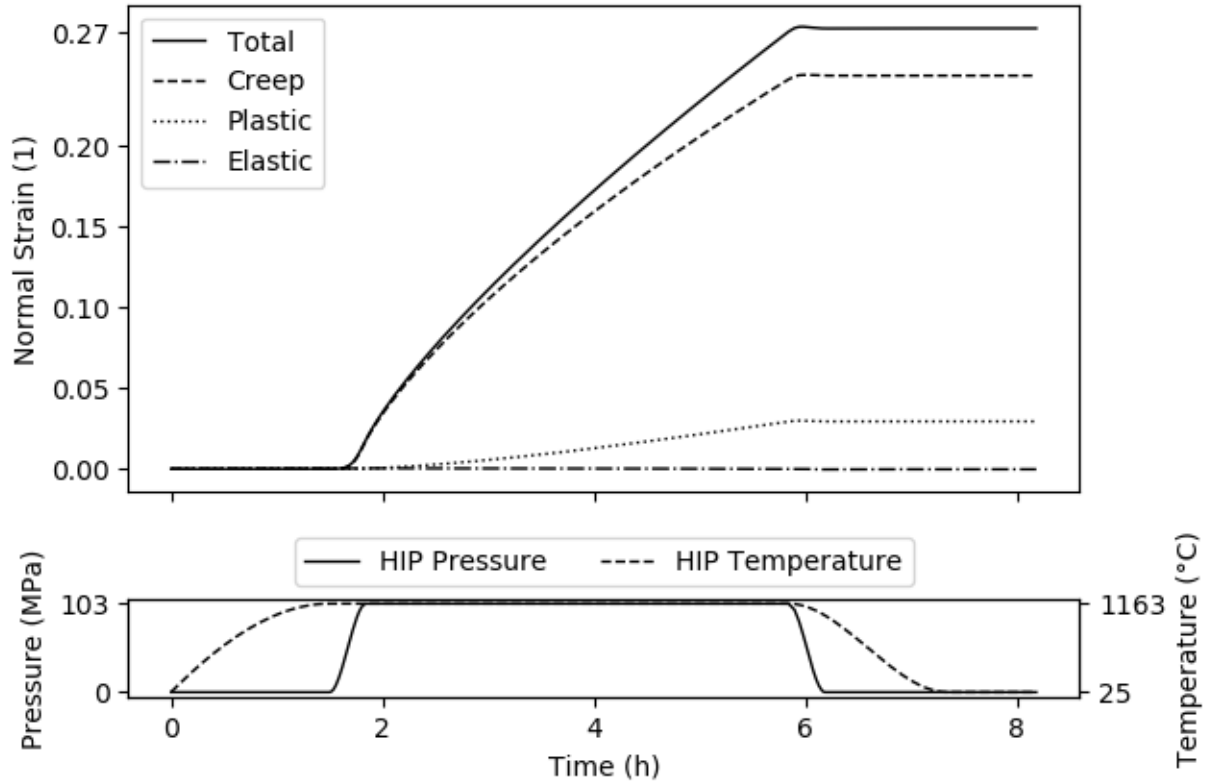
Figure 14: Baseline case normal strain components at pore wall. Note total deformation is dominated by creep.

Figure 15 provides a better visualization of the normal pore wall plastic and elastic strain components. Note that the magnitude of the plastic strain is much greater than the elastic strain; axes scaling was differed in order to improve visualization of the trends of both components. Elastic strain is initially and briefly the dominant strain mode, but only until plastic and creep deformation becomes significant. Elastic strain slowly decreases throughout the hold, and sharply decreases as the HIP pressure and temperature ramps back to ambient commence. The elastic relaxation partially responsible for the slight increase in pore volume and decrease in pore pressure is apparent. There is some residual normal elastic strain remaining at the pore wall after the HIP cycle has concluded and is stable. This dimensionless residual elastic strain is approximately -0.00018 with the negative sign indicating a strain in the outward (expanding) direction.
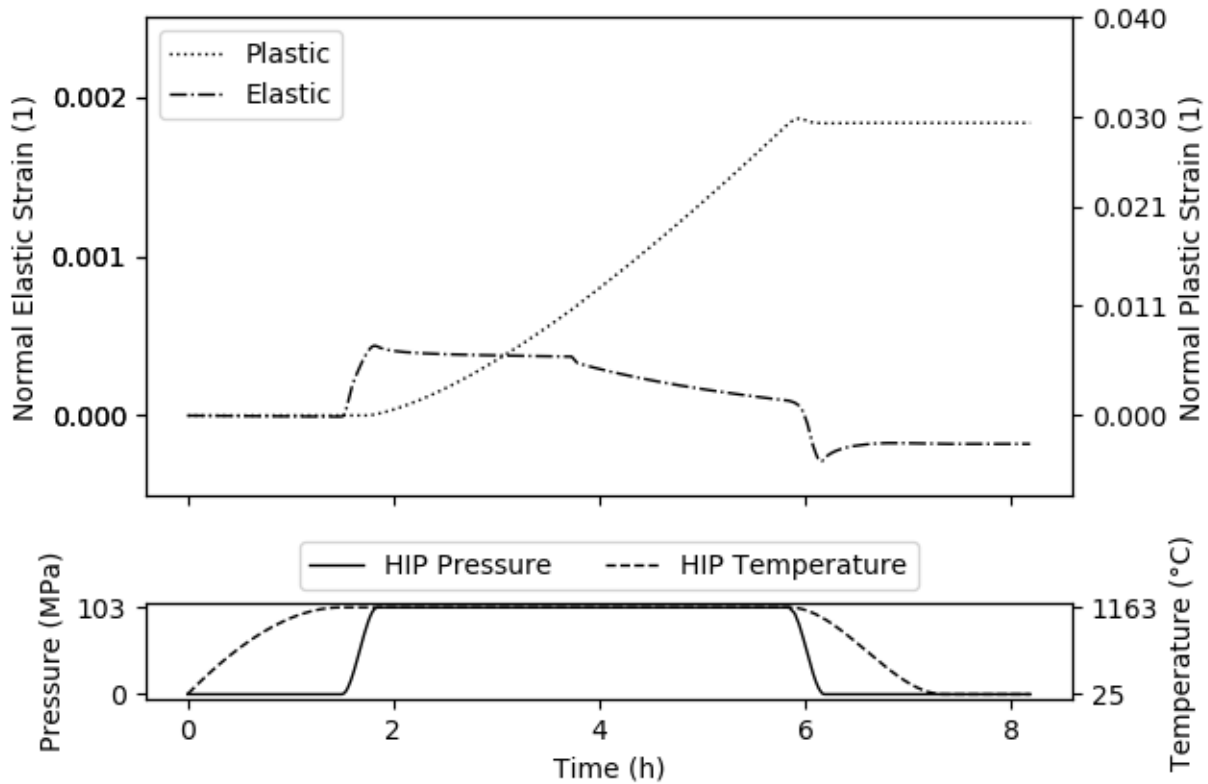
Figure 15: Baseline case normal elastic and plastic strain components at pore wall. Note significant adjustment to axes scales for visualization purposes.

The representative volume length parametric study varies the length of the cubic representative solid volume surrounding the pore to ensure that the representative volume selected for analysis is sufficiently large such that varying its size does not affect the predicted pore closure resulting from deformation of the solid volume. In order to ensure that the representative volume selected was large enough to be held constant during the separate initial pore diameter parametric study (see Table 7), the largest pore diameter in that study – 800 μm – was selected as the control value for this representative volume length study. The other parameters for the representative volume length study are held at baseline conditions. The results of this study indicate that the baseline representative volume length value of 0.5 m is sufficiently large such that the representative volume does not bias pore closure predictions even for the 800 μm pore. These results are shown in Figure 16. Excluding the effect of proximity of load surfaces and other defect features is a modeling assumption. A sufficiently large representative volume ensures that load stresses are distributed around the pore such that the arbitrary selection of distance between the load surfaces and the pore does not influence predictions. These results indicate that, for an 800 μm pore, if the pore is located less than approximately 0.05 m from defect or loading surfaces the pore would close more fully than if it was located further away. This may indicate some critical distance, however, there are meshing considerations that may influence this value somewhat and are discussed shortly.

These results indicate that a much smaller representative volume could have been selected for the baseline case where the pore diameter was 100 μm. The impact of selecting such a large baseline representative volume is expected to be minimal and would solely impact solution time as a larger geometry needs to be resolved. However, stress and strain gradients are highest near the pore which is where mesh density is highest. Although decreasing the representative volume size could potentially permit fewer total elements in the model, decreasing the representative volume size also brings the load surfaces closer to the pore. Holding mesh count constant for this parametric study allowed for higher mesh density near the load surfaces which may have partially contributed to the flatness of the curve in Figure 16 down to around 0.05 m. In the interest of time, further assessment was not conducted, and the baseline case was deemed sufficient.
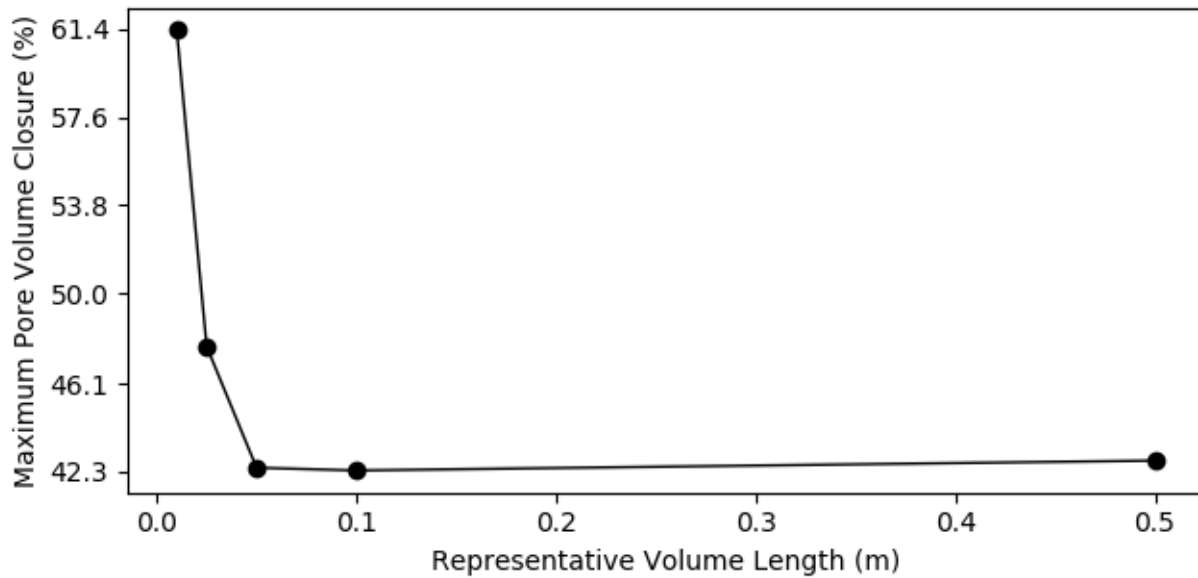
Figure 16: Representative volume length parametric study results indicate that the baseline value of 0.5 (m) is sufficiently large.

The pore diameter parametric study was conducted to show how the final pore size varies over a range of initial diameters. The other parameters for this study were held at baseline settings. As expected, relative measures of pore closure were independent of initial pore diameter and absolute measures were not. Two relative effects of pore diameter, maximum pore volume closure percentage and maximum pore gas pressure, are illustrated in Figure 17. Maximum pore closure volume percentage is a metric which measures final pore volume relative to initial pore volume. Strain is a physical phenomenon which is proportional to the initial size. Consequently, maximum pore closure volume percentage is by definition constant across initial pore diameter if the strain rate is constant. This is the case since strain rate varies only with other parameters such as HIP temperature which were held constant during this parametric study. Maximum gas pore pressure is also proportional as it is a direct consequence of change in pore volume from the initial volume because other parameters were held constant. Figure 18 shows maximum pore diameter as an example of an absolute measure of pore closure. Maximum pore diameter does vary with initial pore diameter because in order to achieve the same proportional change in a large vs. a small pore a large vs. a small absolute change would be required.
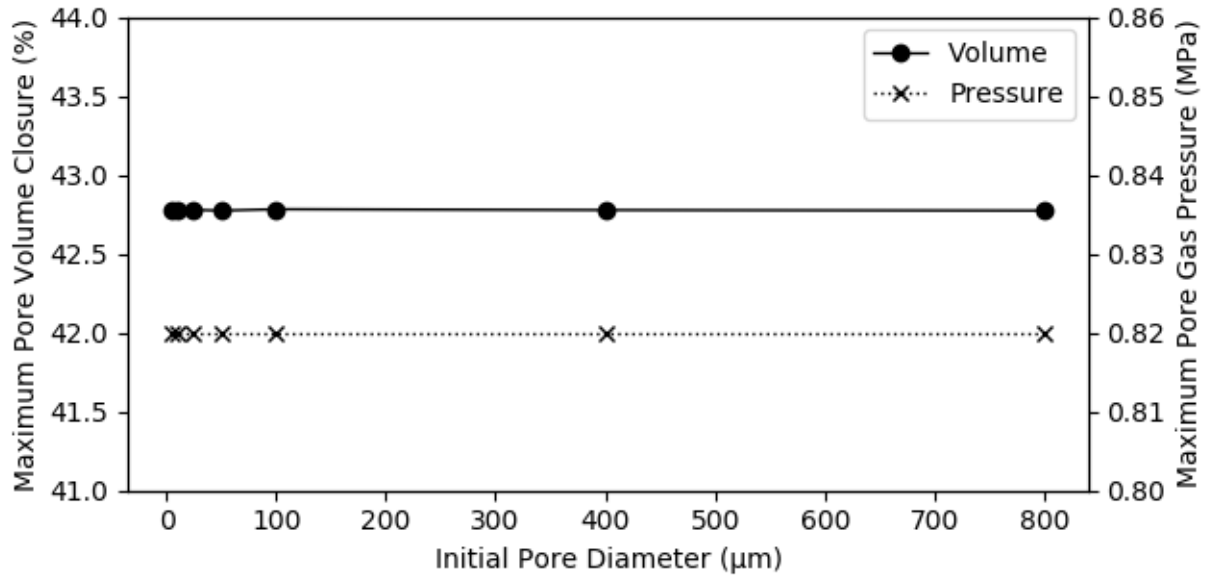
Figure 17: Relative effects of pore closure are independent of initial pore diameter as expected.
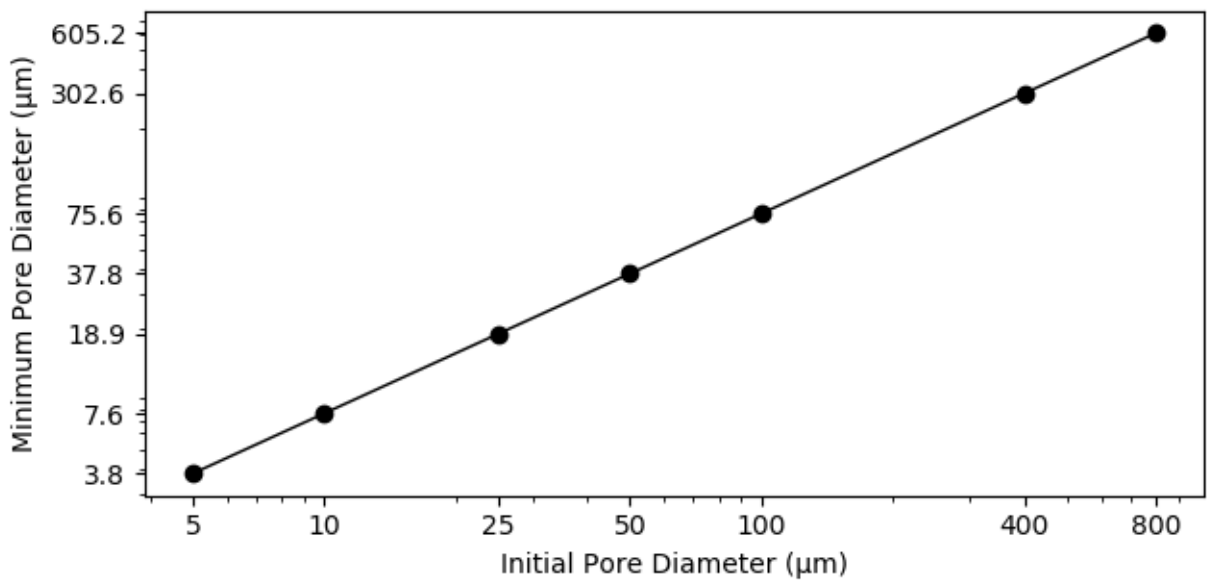
Figure 18: Log - log plot showing maximum pore diameter as initial pore diameter is varied. Axes labels correspond to actual values.

Mesh count, described in detail in the model overview section, indicates mesh density. The purpose of this study is to determine that the baseline mesh density is high enough to ensure that model predictions are mesh independent. In order to ensure that the mesh count selected was large enough to be held constant in the separate initial pore diameter parametric study (see Table 7), the smallest pore diameter in that study – 5 μm – was selected as the control value for pore diameter in this mesh count study. The other parameters for this study were held at baseline settings. Figure 19 illustrates the stability in predicted maximum pore volume closure percentage for mesh count values between 10 and the selected baseline value of 70. Increased mesh count values come at an increased computational cost. It is possible that mesh count values larger than 70 could achieve further stability in model predictions; however, mesh count values between 40 and 70 predicted maximum pore volume closure percentage values which varied by only 0.02%.
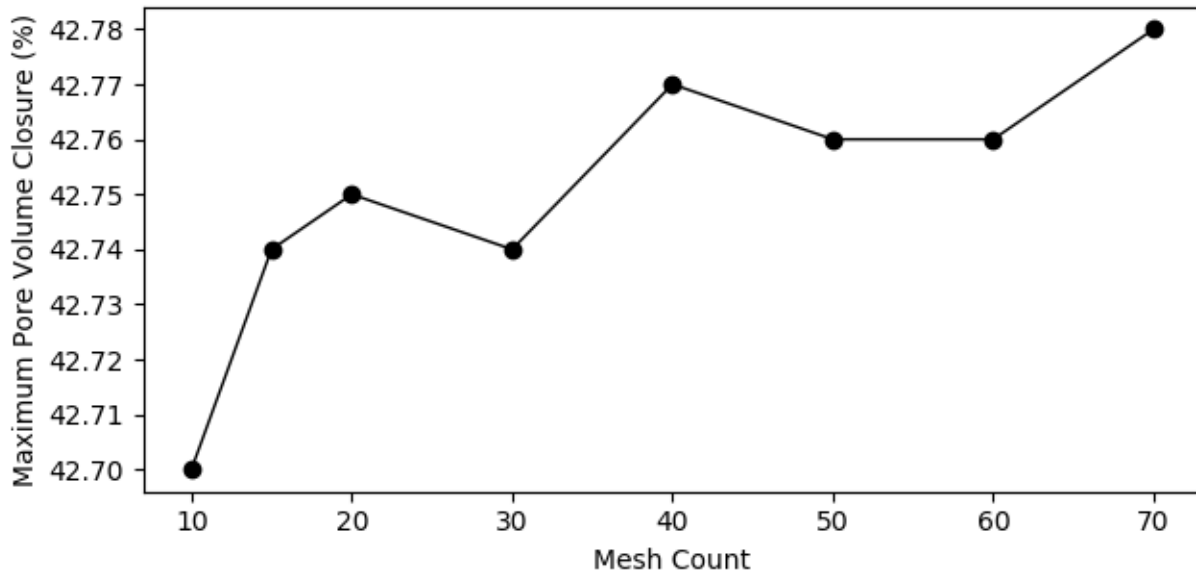
Figure 19: The baseline mesh count of 70 is high enough for mesh independent predictions. Note the scale of the dependent variable axis.

The purpose of the HIP hold pressure parametric study is to assess the effect of varying HIP hold pressure against the baseline case on the predicted pore closure resulting from deformation of the solid volume. The HIP hold pressure was varied +/- 10% of the baseline value. The other parameters for this study were held at baseline settings. The results of this study are shown in Figure 20. There is a clear trend toward increasing pore closure as HIP hold pressure increases. This is to be expected as the HIP hold pressure represents the external loading applied to the model which impacts all strain components contributing to deformation. Within the bounds of the pressure variation tested, the increasing trend appears to be linear. This is also reflected in Figure 21 which shows the pore closure over the course of the HIP cycle for the hold pressure levels tested. The pore closure transient rates are similar in shape with a roughly linear increase overall as pressure is increased.
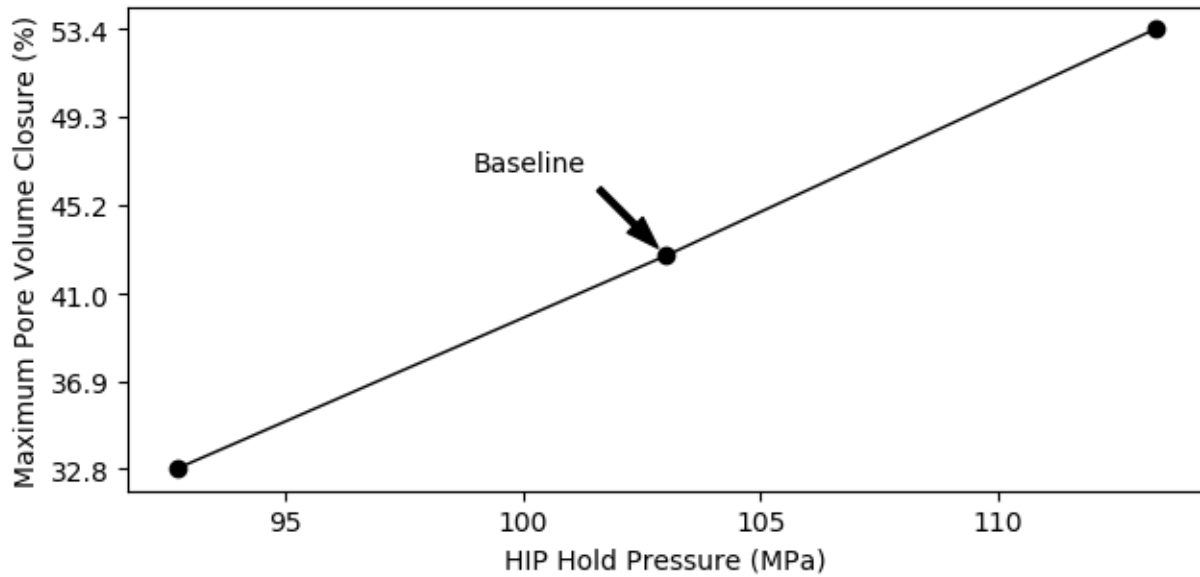
Figure 20: The effect of varying HIP hold pressure on pore closure at baseline conditions. Note the roughly linear increase in closure rates as pressure is increased.
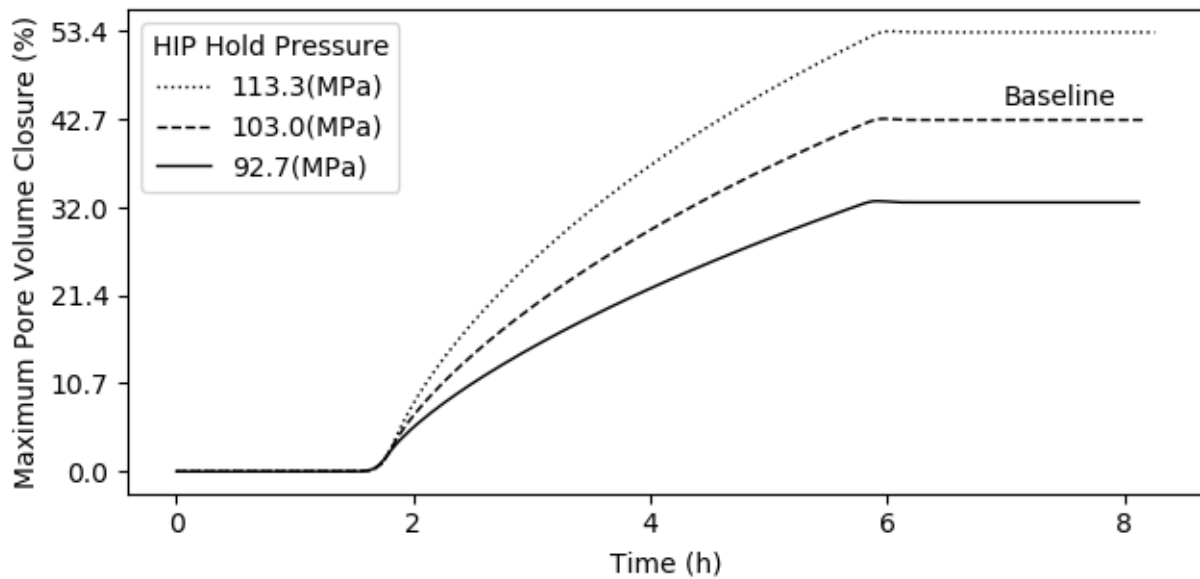
Figure 21: The effect of varying HIP hold pressure on pore closure transience.

In contrast to HIP hold pressure, varying HIP hold temperature has a more significant and non-linear effect on pore closure. In this parametric study, HIP hold temperature was varied -10%, -5%, 0%, and +5% of the baseline value. The other parameters for this study were held at baseline settings. The results of this study are shown in Figure 22. There is a clear trend toward increasing pore closure as HIP hold temperature increases. This is to be expected as the elastic material properties and the plastic and creep material models are functions of temperature. Increasing temperature effects the elastic material properties notably by decreasing stiffness and increasing density, increases plastic strain via thermal softening, and increases creep strain rate via an Arrhenius type temperature dependence. Within the bounds of the temperature variation tested, the increasing trend appears to be non-linear. This is also reflected in Figure 23 which shows the pore closure over the course of the HIP cycle for the hold temperature levels tested. The pore closure transience rates changing in shape with a non-linear increase overall as temperature is increased.
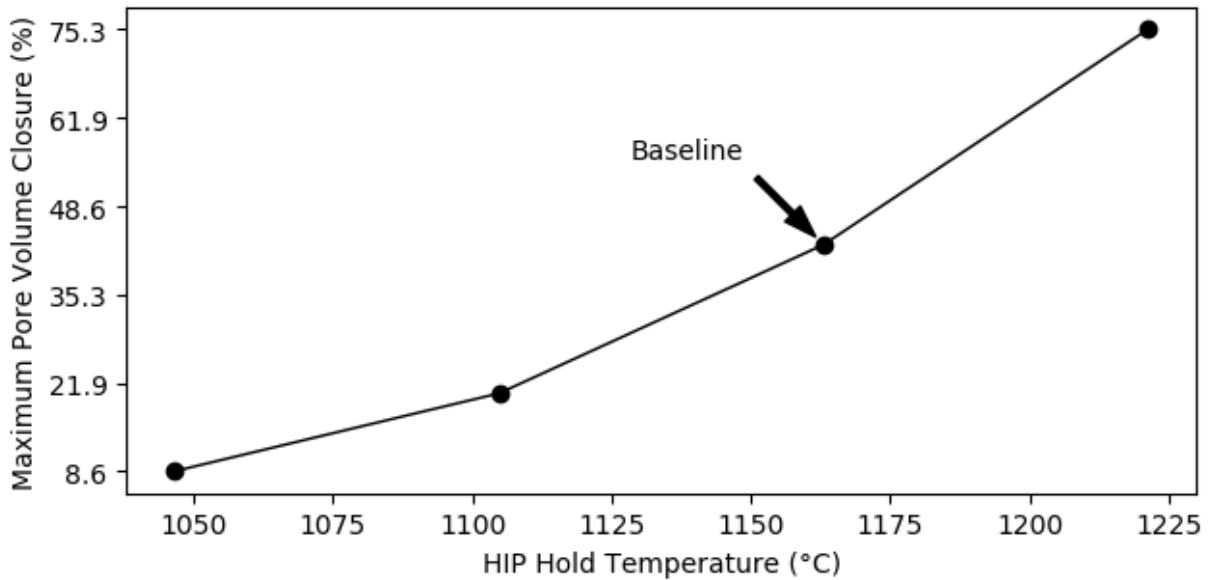
Figure 22: The effect of varying HIP hold temperature on pore closure at baseline conditions. Note the non-linear increase in closure rates as temperature increases.
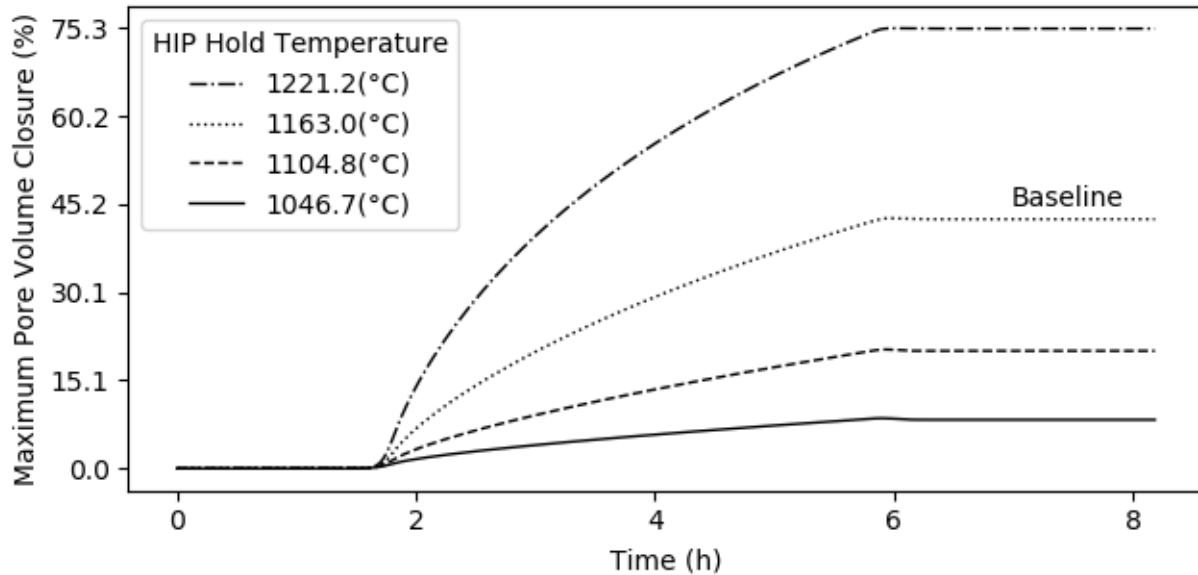
Figure 23: The effect of varying HIP hold temperature on pore closure transience.

The purpose of the HIP hold time parametric study is to assess the effect of varying HIP hold time against the baseline case on the predicted pore closure resulting from deformation of the solid volume. The HIP hold time variation was provided by the project. The other parameters for this study were held at baseline settings. The results of this study are shown in Figure 24. There is a clear trend toward increasing pore closure as HIP hold temperature increases. This is to be expected as creep dominates deformation during the hold, and the HIP hold pressure represents the external loading applied to the model which impacts all strain components contributing to deformation. Within the bounds of the pressure variation tested, the increasing trend appears to be linear. This is also reflected in Figure 21 which shows the pore closure over the course of the HIP cycle for the hold pressure levels tested. The pore closure transience rates are similar in shape with a roughly linear increase overall as pressure is increased.
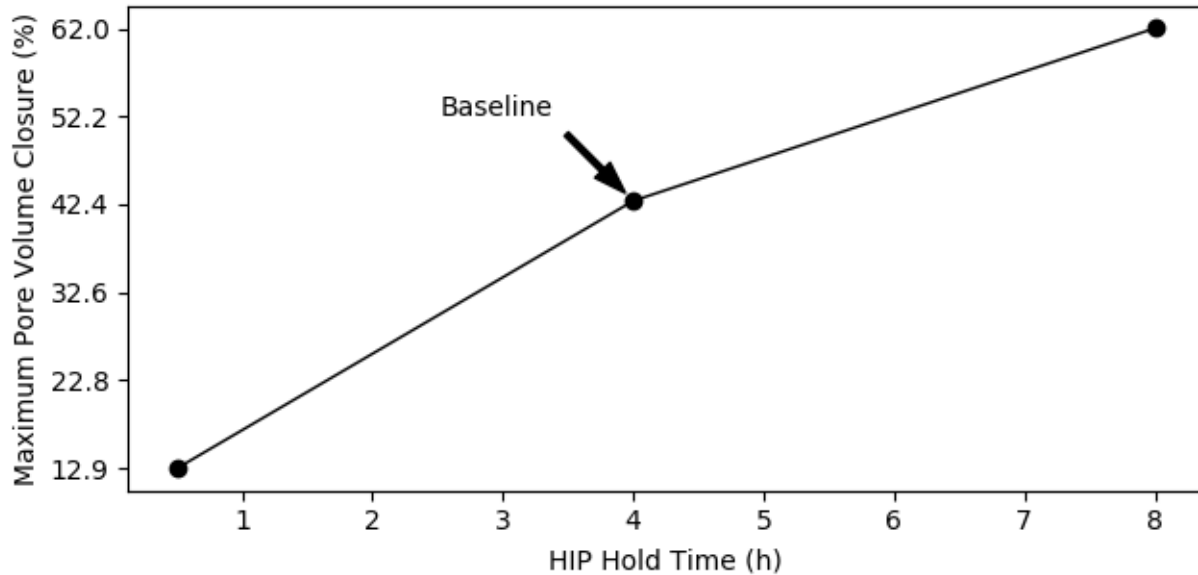
Figure 24: The effect of varying HIP hold time on pore closure at baseline conditions. The trend primarily follows the baseline closure rate with each test point indicating the extent of closure at the time the hold was terminated for that case as closure primarily occurs during the hold.

In order to assess the effect of the 2-D geometry and plane strain assumption on the results, a 3-D case was run for comparison. Given time constraints a single 3-D model case was run; the geometry selected was a spherical pore which was simulated as a 1/8th model reduced about the symmetric x, y, and z planes. The pore volume closure percentage results of the 3-D spherical pore model at baseline HIP conditions are compared to the 2-D baseline case in Figure 25.
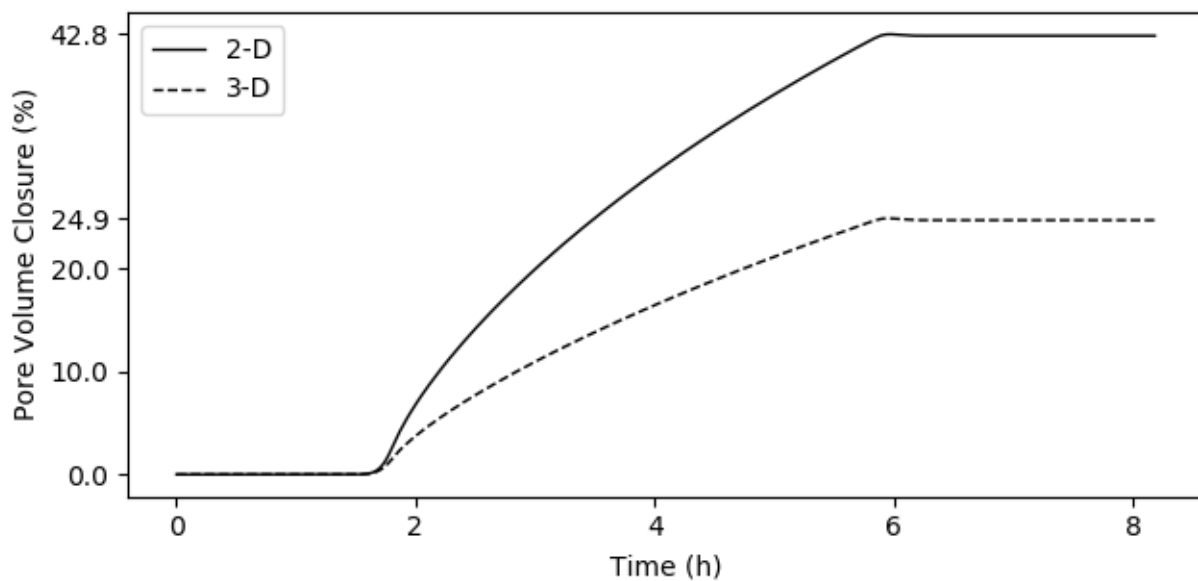
Figure 25: 2-D and 3-D model pore closure at baseline conditions.

As is apparent from the results, the 3-D spherical pore model achieves significantly less pore closure than the 2-D round (pseudo-cylindrical) pore at the same conditions. It should be noted here that although the 2-D model employs a plane strain assumption – out of plane strains are null – the out of plane stress is still calculated with the assumption that the planar thickness is 1 m. This is akin to a 1 m thick block with an open cylindrical hole bore for the purposes of stress calculations. A close inspection of the strain components show that both models experience similar strain transience and strain component fractions (total, creep, plastic, and elastic); however, the amplitude was lower in the 3-D model with total strain about 39% less than in the 2-D case. A sphere is an ideally stable shape due to its complete symmetry, so resistance to closure should be expected. It appears likely the spherical shape is responsible for the decrease in closure due to the broader distribution of stress around the pore. This is especially true for shear stress which is negligible in the 2-D case. With stress distributed around the sphere, less of the overall load would be expressed normal to the pore wall, reducing pore closure. Components of the deviatoric stress tensor are shown for both the 2-D and 3-D models in Figure 26 at a point on the pore wall where x is normal. Note the relative similarity of the x component between the models, but the very large difference in the shear components xy and xz.
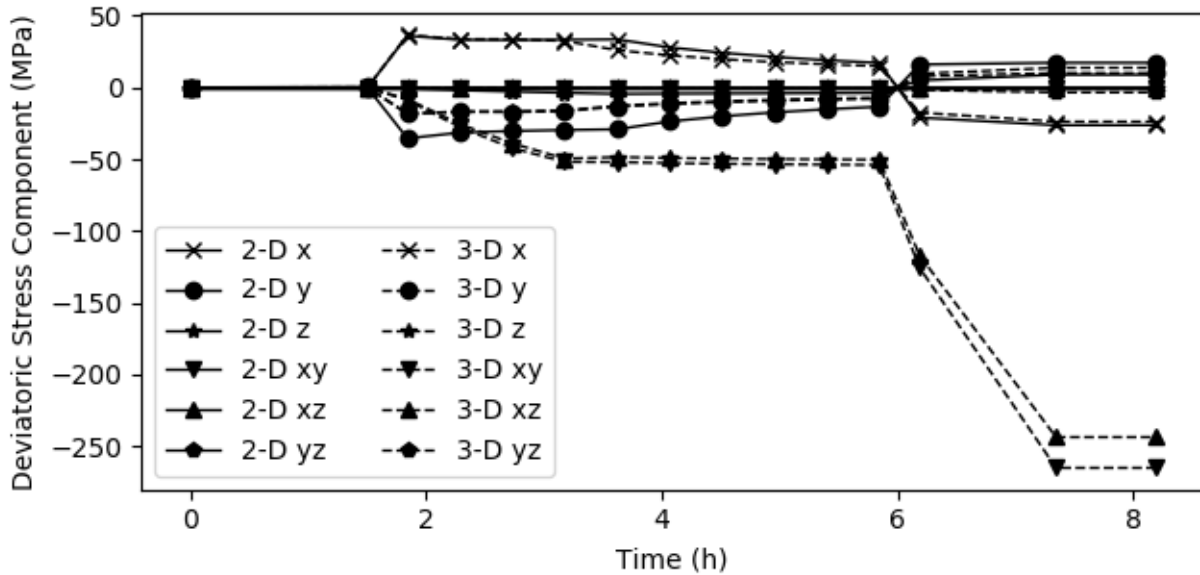
Figure 26: Components of the 2-D and 3-D model deviatoric stress tensors where x is normal to the pore wall. Note the similarity in the x component but the large differences in the xy and xz shear.

As a verification, a ¼ version of the 2-D baseline model reduced about the symmetric x, and y axes was run with nearly identical results to the standard baseline case (pore closure percentage predictions were within 0.00003%). It is not clear to what extent the differences in mesh and shape of the representative solid volume had on results.

6.0 DISCUSSION

A primary general finding from this analysis is the importance of correct plasticity and creep material models. This is especially true for the creep model which, in the baseline case, accounts for 87.7% of the total strain at the conclusion of the HIP cycle. There are two primary factors dictating the creep behavior of IN718: microstructure and creep environment. Both microstructure (grain and precipitate particle size) and environment (temperature and loading) significantly influence the creep mode and creep strain rates, and the creep material model should be capable of accurately describing the effects of these factors. Ultimately, this ability is enabled by choosing a creep model which can account for the material specific creep modes of IN718 and choosing parameters for the model that are most relevant to the expected microstructure and environmental conditions. The predictions in this analysis likely contain significant error largely due to a need to rely on creep model parameter values derived from published rather than application specific IN718 microstructures and environmental conditions. Recommendations for improving the predictions are further discussed below and in Future Work section 7.2.

For this analysis, time and laboratory access restrictions resulted in the selection of the Norton power law creep model and model parameters based on published materials test data. The Norton creep model was a good starting point and is widely used to generally model creep deformation in metals, but any further investigations should review and compare other creep models applicable to precipitation hardened alloys such as IN718. Candidate models are available in literature such as in (Chaturvedi and Han 1989), (Nguyen, et al. 2017), and (Swindeman and Swindeman 2008).

Of special importance, further investigations should include resources for acquiring microstructure and environment specific compression creep test data such that more relevant model parameters can be implemented. In the current analysis, initial attempts were made to source Norton power law creep model parameters for IN718 directly from literature. There are resources for creep model parameters, such as (Saberi, et al. 2020); however, none were located which were developed to model creep behavior near the relevant HIP hold conditions for this study. Consequently, a strategy was employed to source IN718 creep test data from literature and utilize linear regression analysis to fit the Norton equation form to the data and determine the correct model parameters.

Creep data investigated was primarily sourced from (Chavez, et al. 1994) because test conditions were the most relevant to this study of those found in literature. The creep data published in the Chavez paper consisted of 13 tests of 1.27 cm (0.5 in) diameter IN600 rod – annealed for 1 hr at 870 °C and force air cooled – in tension in an Argon atmosphere at conditions ranging between 732 – 1093 °C and 14 – 173 MPa. The data was presented primarily as transient functions which showed short initial secondary creep regions followed by large tertiary curves leading to failure. Initial attempts to employ the transient creep data, by adopting a time-dependent Norton-Bailey creep function, were abandoned. Although the data fits using the Norton-Bailey approach described the data acceptably well, when employed in the model creep strain rates were produced which were unbelievably fast at well over 1000 1/s. For example, a 10 µm pore at baseline conditions achieved nearly 80% of full closure after only 15 mins from the commencement of the HIP pressure ramp, causing the simulation to diverge more than 5 mins before the HIP hold began. It is possible that this phenomenon was observed because the Chavez creep tests were conducted in tension, and as specimen approached failure a much more significant and dominant tertiary creep component was reported than would be observed in compression. Consequently, linear extrapolations of minimum creep rates reported by the author to estimate secondary creep rate components were used in the analysis which are shown with the resulting Norton model fit in Figure 3. It should be noted that although the reported creep data temperature and pressure ranges were reasonably applicable to the HIP hold conditions, the individual data points were at pressure and temperature combinations that were not. Baseline HIP temperature and pressure for this study were 1163 °C and 103 MPa. The most relevant test data point by pressure was 93.6 MPa but test temperature was only 732 °C; by temperature the best point was 1093 °C but pressure at this point was only 22.2 MPa. Consequently, the Norton fit must be extrapolated well beyond the range of the provided test data; because creep is highly sensitive to changes in temperature and pressure this model is likely not accurate and would benefit from test data conducted at expected hold conditions. Extrapolations of the Norton model from the temperature and pressure environment relevant to the test data up to the HIP hold temperature and pressure are shown in Figure 27.
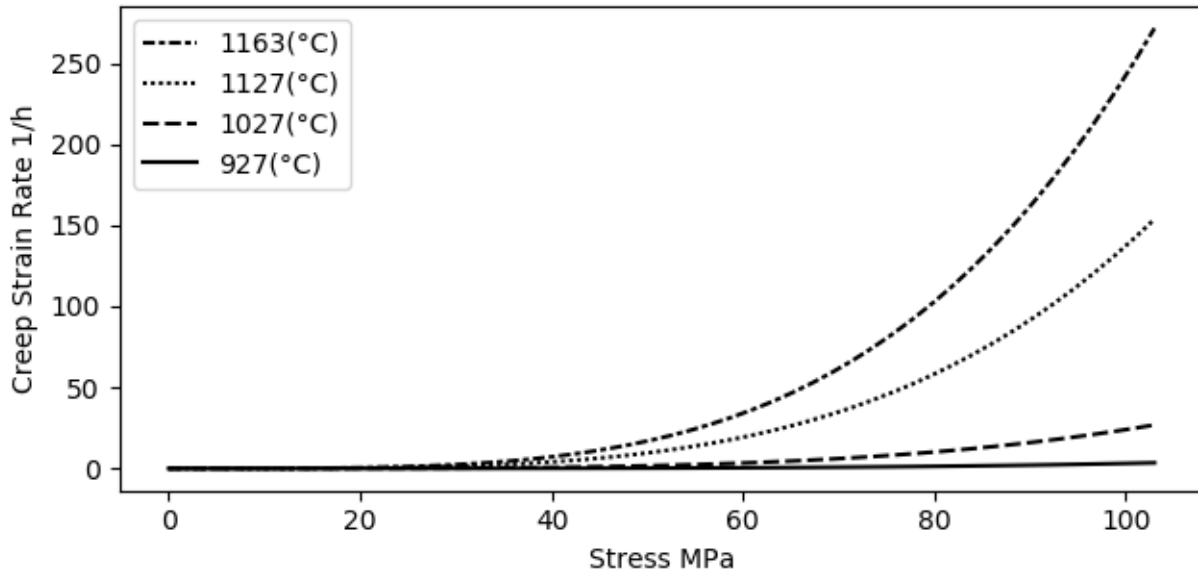
Figure 27: Norton creep model extrapolated to baseline HIP hold conditions (1163 °C, 103 MPa). The most relevant fit data by pressure was 93.6 MPa at 732 °C and by temperature 1093 °C at 22.2 MPa.

In addition to creep test data taken at relevant environmental conditions, specimen microstructure should also be considered. The effect of heat treatment (grain size) and aging (precipitate particle size) on creep characteristics of IN718 was studied by (Chaturvedi and Han 1989). In the Chaturvedi paper, IN718 specimens with a cross section of 1.3 x 5.5 mm (.05 x .22 in) were annealed after machining to various temperatures between 970 – 1100 °C and water quenched in order to produce different grain sizes ranging between 10 – 100 µm. Creep rate testing was conducted at 600 – 650 °C and 650 – 820 MPa on these specimen, and two important findings were reported. First, IN718 undergoes a transition from diffusion (linear) to dislocation (power law) type creep within this test range. Consequently, although the baseline HIP hold conditions are well into the region of power law creep, the Norton power law model may not correctly predict creep rates in the HIP pressure and temperature ramp as the Norton model assumes a constant exponent. Second, Chaturvedi found that grain size has a significant impact on creep rate. In the linear region, creep rate decreases with increasing grain size; in the power law region, creep rate increases with increasing grain size. At the test point which was most applicable to power law creep, a 152% difference in creep rate was reported between the samples with the smallest and largest grain size. Additionally, specimen were aged for 10 – 15 hours at 725 °C in order to produce various precipitate particle sizes and then tested at 800 °C and between 690 – 815 MPa. There was a clear minimum creep rate, with over and under aging (larger and smaller particles) increasing creep rate up to 50x (for the 815 MPa case). It is clear that microstructure significantly influences creep rate; therefore, commercial IN718 which is strengthened by about 17% precipitates by volume is likely a poor indicator of the creep behavior of as-built IN718 with inconsistent and large grained anisotropic microstructure. In summary, compression test data taken at environmental conditions and using samples with microstructures relevant to the study would significantly improve pore closure prediction accuracy.

The accuracy of the plasticity model is also of interest, although of less importance than creep in the correctness of the overall model. The Johnson-Cook plasticity model was selected for this analysis primarily because the Johnson-Cook model is commonly used and published parameter values for IN718 are available including in (Farahani, Ketabchi and Zangeneh 2017), (Grzesik, Niestony and Laskowski 2017), and (Iturbe, et al. 2017). The parameters chosen for this analysis were taken from (Iturbe, et al. 2017) primarily because model parameters in this paper were generated using coaxial compression tests at temperatures up to 1050 °C at a stress of 200 MPa and strain rates up to 100 1/s which was the most relevant conditions to the current study that was found in literature. The Johnson-Cook model as employed in the current analysis is shown compared to test data provided in the paper at the most relevant set of conditions over the range of tested strain rates can be seen in Figure 28.
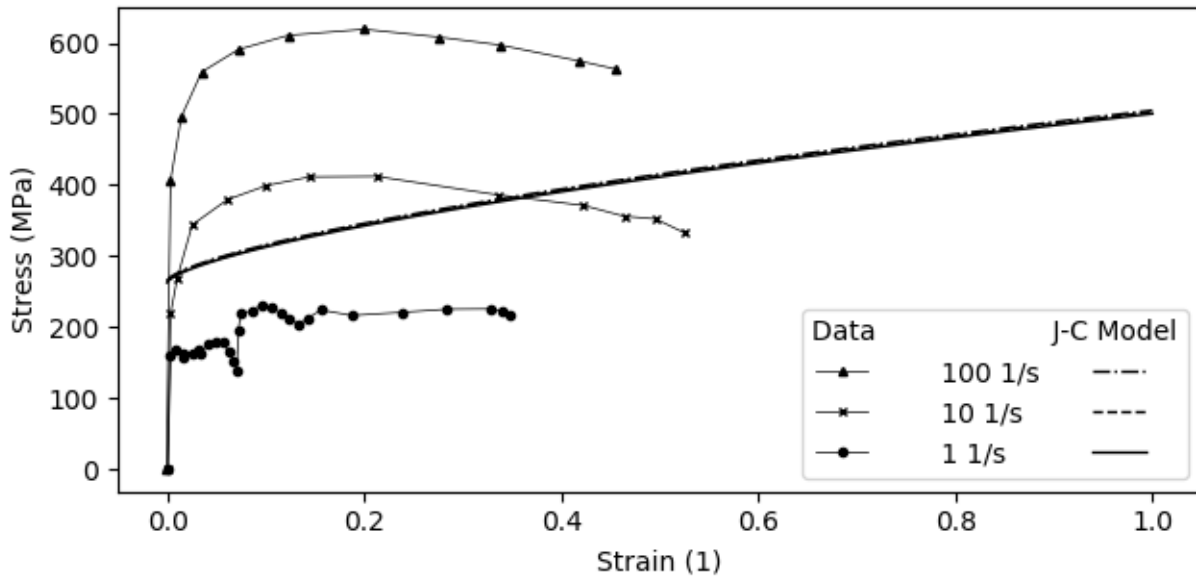
Figure 28: Axial compression test data from (Iturbe, et al. 2017) and utilized Johnson-Cook plasticity model at 1050 °C over a range of strain rates in published data most applicable to the current study. Note the independence of the model over strain rate.

(Iturbe, et al. 2017) point out that a severe degradation in IN718 mechanical properties are observed with time as temperature exposures exceed approximately 650 °C largely due to the transformation of the metastable γ" phase which is a primary IN718 strengthening precipitate. This microstructural transition serves as a temperature dependent properties delineation point for both strain and strain rate. Below this temperature, strain increase resulted in work hardening until shear failure; strain rate had a negligible influence on properties in this regime. Above this transition temperature, strain rate hardening was initially observed due to dislocation pileup, but additional strain resulted in softening likely due to dislocation mobility resulting from thermally activated phenomenon; strain rate hardening became important due to the increasingly viscous behavior of the alloy. As can be observed in Figure 28, the Johnson-Cook model behavior employed in this study embodied the low temperature characteristics (strain hardening and negligible strain rate effects) even at 1050 °C where the test data clearly indicated the higher temperature characteristics. Due to time constraints, the traditional Johnson-Cook parameters provided in the Iturbe paper were used, except for the adoption of a novel thermal softening term. This novel thermal softening term is continuous over the reported test range (21 – 1050 °C) and this exponential term is an improvement on the traditional linear approach which is less well suited to the behavior of IN718. Further investigations may benefit from a modified plasticity approach which better accounts for the obvious temperature dependent strain and strain rate effects of IN718.

The importance of correct creep and plasticity model implementation has been emphasized; additionally, it may be valuable to provide evidence to guide prioritization of any future material model parameter test regimen. First, improving the creep model should be prioritized over the plasticity model. As previously substantiated, the contribution of creep to overall deformation is significantly greater than plasticity. Second, correctness of temperature dependent properties and temperature control should be prioritized over strain or strain rate in any future creep or plasticity test efforts. Results from this analysis show that deformation has a higher sensitivity to, and non-linear dependence, on temperature compared to loading (pressure). This can be seen in Figure 29 which compares the results of the HIP hold temperature and HIP hold pressure parametric studies.
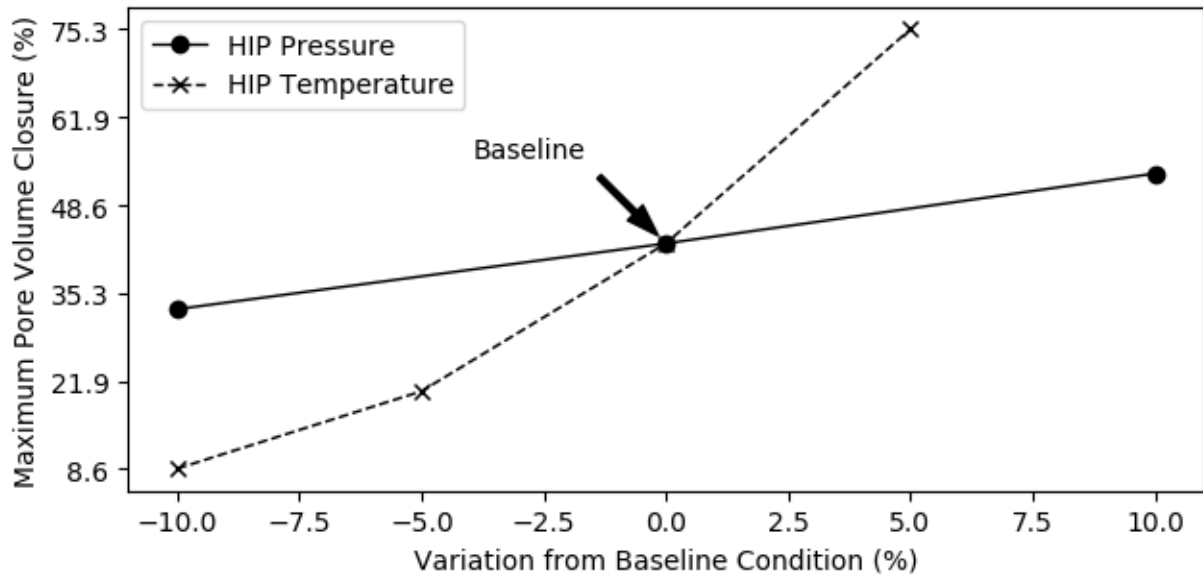
Figure 29: Pore closure (primarily due to creep) is more sensitive to changes in HIP temperature than HIP pressure around the baseline condition.

It is important to emphasize the preliminary nature of the analysis, and that a firm understanding of model assumptions should be considered when interpreting the results. Parametric study of the size of the representative volume was conducted to ensure that a sufficiently large volume was selected for the analysis such that the effects of pore wall proximity to surfaces could be controlled for. However, pores in real materials will be located near other pores and possibly loading surfaces; this can have a significant impact on the stress distribution in the solid material and consequently on deformation. As seen in Figure 16, for the baseline case conditions, a pore located less than approximately 0.05 m from a surface or other defect may experience effects which could change the predicted pore closure behavior outlined in this work.

Future efforts continuing this initial work may benefit from investigating the possibility of implementing thermal expansion coefficient material properties data rather than temperature dependent density as was done in this work. In retrospect, thermal expansion coefficient material properties data would be a more accurate property to implement as it was directly measured; temperature dependent density was calculated using thermal expansion coefficient data. Further, thermal expansion was not implemented into the structural mechanics approach; therefore, volume changes due to temperature dependent density variation was not accounted for.

7.0 CONCLUSIONS

A thermo-mechanical model was created to study the percentage of pore closure for IN718 in 2-D and 3-D as a function of the HIP process parameters. A single symmetric pore was modeled and a representative volume was identified for the surrounding solid material domain size. Ideal pore geometry was utilized for capability development, and the study of irregularly shaped pores is identified for future work. Creep and plastic deformation behavior for IN718 was estimated based on available data and identified as critical model inputs. Future work in this area should primarily focus on collecting relevant creep and plasticity material parameters at the thermal and mechanical environmental conditions of interest and then collecting and applying validation data to assess model accuracy. Secondary objectives may be to: investigate methods of implementing contact in full pore closure; allow for irregular pore geometries; and assess the impact of microstructure effects, pore gas diffusion, and surface tension.

7.1 Lessons Learned

The creep model is a significant input for the pore closure analysis. Material data at the process conditions of interest was not available. Extrapolation was needed, and the creep material behavior was a critical factor for predicting the amount of pore closure given the pressure, temperature, and time of the HIP process. Material testing for IN718 to help define creep behavior at the conditions of interest is needed to improve the model accuracy. Additionally, validation data which shows the amount of pore closure under various HIP process conditions is needed for comparison with model predictions. Finally, the spherical pore geometry chosen for this study provided an ideal case for creating the analysis capability. The spherical geometry assumption leads to pore closure which reduces to a point and avoids contact. In general, the pores will be irregularly shaped which requires contact to be implemented for the pore surface.

7.2 Future Work

Future work identified from this study includes generating validation data, creep testing to generate input for the material model, and further improvements that increase model fidelity which are described now.

Characterization of pores before and after HIP is needed to provide validation data for the analysis effort. Due to the current pandemic, lab access is restricted. Consequently, the study of seeded defect specimens originally planned as part of this activity is listed as future work.

Future efforts should consider implementation of temperature dependent coefficient of thermal expansion (CTE) solid material properties rather than calculated temperature dependent density.

As identified in Section 2.3, the creep material model is critical to modeling the pore closure during HIP of IN718. Creep tests at the relevant stress and temperatures identified for the HIP process are needed for development of a material model which accurately represents the creep behavior for the material and conditions of interest.

While this study focused on ideal pore geometry, irregularly shaped pores can be studied to understand the impact of pore shape during the HIP process. Representative pore geometry can be constructed, or CT data can be utilized as input to the pore closure model. Additionally, contact can be implemented for the pore surfaces which becomes necessary for irregularly shaped pores.

Finally, the bond condition and creep behavior can be modeled to study post HIP pore closure.

8.0 ACKNOWLEDGMENTS

9.0 REFERENCES

Atkinson, H. V., and S. Davies. 2000. "Fundamental Aspects of Hot Isostatic Pressing: An Overview." *Metallurgical and Materials Transactions A* 2981-3000.

Chaturvedi, M. C., and Yafang Han. 1989. "Creep Deformation of Alloy 718." *The Minerals, Metals & Materials Society,* . The Minerals, Metals & Materials Society. 489 - 498.

Chavez, S. A., G. E. Korth, D. M. Harper, and T. J. Walker. 1994. "High-temperature tensile and creep data for Inconel 600, 304 stainless steel and SA106B carbon steel." *Nuclear Engineering and Design* 351 - 363.

COMSOL Multiphysics (R) v. 5.5. 2019. "Structural Mechanics User's Guide." Stockholm.

Du, Y., and et al. 2019. "Theory and Technology of Sintering, Thermal and Thermochemical Treatment: Consolidation and Simulations of Hot Isostatic Pressing of Selective Laser Sintered Stainless Steel Parts." *Powder Metallurgy and Metal Ceramics* 249-256.

Epishin, A., B. Bokstein, I. Svetlov, B. Fedelich, T. Feldmann, Y. Le Bouar, A. Ruffini, A. Finel, B. Viguier, and D. Poquillon. 2018. "A Vacancy Model of Pore Annihilation During Hot Isostatic Pressing of Single Crystals of Nickel-Base Superalloys." *Inorganic Materials: Applied Research* 57-65.

Farahani, H. K., M. Ketabchi, and S. Zangeneh. 2017. "Determination of Johnson–Cook Plasticity Model Parameters for Inconel718." *Journal of Materials Engineering and Performance.*

Finfrock, C., and et al. 2018. "Effect of Hot Isostatic Pressing and Powder Feedstock on Porosity, Microstructure, and Mechanical Properties of Selective Melted AlSi10Mg." *Metallography, Microstructure, and Analysis* 443-456.

Grzesik, W., P. Niestony, and P. Laskowski. 2017. "Determination of Material Constitutive Laws for Inconel 718 Superalloy Under Different Strain Rates and Working Temperatures." *Journal of Materials Engineering and Performance* 5705–5714.

Iturbe, Ariane, Eliane Giraud, Exabier Hormaetxe, Ainhara Garay, Guénaël Germain, Koldo Ostolaza, and Pedro José Arrazola. 2017. "Mechanical characterization and modelling of Inconel 718 material behavior for machining process assessment." *Materials Science and Engineering: A* 441-453.

Joo, S-H, and et al. 2014. "Finite Element and Experimental Analysis of Closure and Contact Bonding of Pores During Hot Rolling of Steel." *Metallurgical and Materials Transactions A* 4002-4011.

Kreitcberg, A., and et al. 2017. "Effect of Heat Treatment and Hot Isostatic Pressing on the Microstructure and Mechanical Properties of Inconel 625 Alloy Processed by Laser Powder Bed Fusion." *Materials Science and Engineering A* 1-10.

Nguyen, C. V., Y. Deng, A. Bezold, and C. Broeckmann. 2017. "A combined model to simulate the powder densification and shape changes during hot isostatic pressing." *Comput. Methods Appl. Mech. Engrg.* 302-315.

2018. *Project 4026: Development of Distortion Prediction and Compensation Methods for Metal Powder Bed Fusion Additive Manufacturing.* Technical Report, America Makes Program sponsored by the Air Force Research Laboratory Under Agreement Number FA8650-12-2-7230.

Saberi, E., S. Nakhodchi, A. Dargahi, and K. Nikbin. 2020. "Predicting stress and creep life in Inconel 718 blade-disk attachments." *Engineering Failure Analysis.*

Sanchez, L., and et al. 2002. "New Viscoplastic Model to Simulate Hot Isostatic Pressing." *Powder Metallurgy* 329-334.

Special Metals Corporation. 2007. "Inconel(R) Alloy 718." Data Sheet (SMC-045).

Swindeman, R. W., and M. J. Swindeman. 2008. "A comparison of creep models for nickel base alloys for advanced energy systems." *International Journal of Pressure Vessels and Piping* 72-79.

Tammas-Williams, S., and et al. 2016. "The Effectiveness of Hot Isostatic Pressing for Closing Porosity in Titanium Parts Manufactured by Selective Electron Beam Melting." *Metallurgical and Materials Transactions* 1939-1946.

Tillmann, W., C. Schaak, J. Nellesen, M. Schaper, M. E. Aydinoz, and K. -P. Hoyer. 2017. "Hot isostatic pressing of IN718 components manufactured by selective laser melting." *Additive Manufacturing* 93 - 102.

United States Department of Defense. 1998. "Metallic Materials and Elements for Aerospace Vehicle Structures." Military Handbook (MILHDBK5H).

Wikman, B., and et al. 2000. "A Combined Material Model for Numerical Simulation of Hot Isostatic Pressing." *Computer Methods in Applied Mechanics and Engineering* 901-913.

REPORT DOCUMENTATION PAGE

Form Approved
OMB No. 0704-0188

1. REPORT DATE *(DD-MM-YYYY)*	2. REPORT TYPE	3. DATES COVERED *(From - To)*
01/05/2021	TECHNICAL MEMORANDUM	01APR2020 - 30SEP2020

4. TITLE AND SUBTITLE

Hot Isostatic Pressing for Reduction of Defects in Additively Manufactured lnconel-718
Preliminary Simulation Approach and Results

5a. CONTRACT NUMBER

5b. GRANT NUMBER

5c. PROGRAM ELEMENT NUMBER

6. AUTHOR(S)

Joshua M. Fody, Christopher G. Lang

5d. PROJECT NUMBER

5e. TASK NUMBER

5f. WORK UNIT NUMBER

811540.19.02.07

7. PERFORMING ORGANIZATION NAME(S) AND ADDRESS(ES)

NASA Langley Research Center
Hampton, VA 23681-2199

8. PERFORMING ORGANIZATION REPORT NUMBER

9. SPONSORING/MONITORING AGENCY NAME(S) AND ADDRESS(ES)

National Aeronautics and Space Administration
Washington, DC 20546-001

10. SPONSOR/MONITOR'S ACRONYM(S)

NASA

11. SPONSOR/MONITOR'S REPORT NUMBER(S)

NASA/TM-20210015451

12. DISTRIBUTION/AVAILABILITY STATEMENT

Unclassified - Unlimited
Subject Category
Availability: NASA STI Program (757) 864-9658

13. SUPPLEMENTARY NOTES

14. ABSTRACT

Selective laser melting (SLM) of Inconel-718 (IN718) is a promising advanced manufacturing technology; however, challenges exist for fracture-critical parts where pores induced during the manufacturing process reduce fatigue life of the material. Hot isostatic pressing (HIP) is a common post processing technique used to reduce the part porosity by exposing parts to high temperature and pressures. Pore closure depends on the pore shape, trapped gas, and HIP parameters, and the process can only be optimized by understanding the effect of these variables. An analysis capability is described to better understand the conditions necessary for pore closure, and the effect of several variables on porosity are explored and compared to a baseline case. The importance of valid material response models is identified as a significant factor in model accuracy; especially the creep material response model which, in the baseline case, predicts that creep strain accounts for 87.7% of the total strain at the conclusion of the HIP cycle. Lessons learned are described, in addition to future work including model validation.

15. SUBJECT TERMS

16. SECURITY CLASSIFICATION OF:			17. LIMITATION OF ABSTRACT	18. NUMBER OF PAGES	19a. NAME OF RESPONSIBLE PERSON
a. REPORT	b. ABSTRACT	c. THIS PAGE			HQ - STI-infodesk@mail.nasa.gov
U	U	U	UU	61	19b. TELEPHONE NUMBER *(Include area code)* 757-864-9658

Standard Form 298 (Rev. 8/98)
Prescribed by ANSI Std. Z39.18